SIMULATION OF SUBSURFACE HYDROGEN STORAGE IN POROUS MEDIA USING CORNER POINT GEOMETRY FOR FIELD APPLICATIONS

T.M.M. van den Dorpel

TU Delft

SIMULATION OF SUBSURFACE HYDROGEN STORAGE IN POROUS MEDIA USING CORNER POINT GEOMETRY FOR FIELD APPLICATIONS

by

T.M.M. van den Dorpel

in partial fulfillment of the degree of Master of Science

at Delft University of Technology,

to be defended publicly on September 19th, 2025 at 10:00 a.m.

Student number:	5174937	
Thesis committee:	Prof. dr. H. Hajibeygi	TU Delft, supervisor and committee chair
	Prof. dr. ir. C. Vuik	TU Delft
	Dr. ir. A. C. Dieudonné	TU Delft
	A. Misaghi Bonabi, MSc.	TU Delft, daily supervisor

TU Delft

DARSim
Delft Advanced Reservoir Simulation

Acknowledgements

This thesis reports the work carried out during the past seven months. Here, I would like to express my gratitude to those who have made these months enjoyable and worthwhile. Hadi, prof. Hajibeygi, from being so welcoming and infectiously enthusiastic during our first meeting, to inviting me to come along to Copenhagen; thank you.
I would also like to thank prof. Vuik and dr. Dieudonné for serving on my thesis committee.
A special thanks to Amin, without whose tireless guidance and supervision, this would not have been possible.
Finally, I want to thank my family, friends, and Romay for their continuous support.

Tim van den Dorpel
Rotterdam, September 2025

Abstract

To mitigate renewable variability, large-scale energy storage systems are necessary to ensure a robust energy network. Subsurface hydrogen storage is considered a promising candidate for large-scale energy storage systems. In this study, corner-point geometry, a standard method for discretizing field-scale subsurface reservoirs, is first validated against Cartesian geometry. Then, the sensitivity of reservoir performance on various reservoir parameters is analyzed. For this purpose, the cyclic operation of a synthetic reservoir is simulated for a period of five years. Several reservoir parameters are then varied, and the resulting changes in recoverability rate are analyzed. From this analysis, it can be concluded that variations in reservoir parameters have the largest impact during the initial cycles of the simulations. However, the results show that reservoir permeability and anticline do have a lasting impact on performance in subsequent injection and production cycles. Finally, the concept of subsurface hydrogen storage in the Johansen formation, located off the coast of Norway, is demonstrated. The results from these simulations show that the injected hydrogen is well-recoverable and underline the importance of careful geological site selection.

Table of Contents

List of Figures

List of Tables

Nomenclature

ABBREVIATION	*Definition*
CCUS	Carbon Capture, Utilization and Storage
CG	Cartesian Geometry
CPG	Corner Point Geometry
FIM	Fully Implicit Method
FVM	Finite Volume Method
NRM	Newton-Raphson Method
PV	Pore Volume
TPFA	Two-Point Flux Approximation

SYMBOL	*Definition*	*Unit*
A	Surface area	m^2
D	Darcy	$9.869233 \cdot 10^{-13}$ m^2
g	Gravitational acceleration	9.81 $m \cdot s^{-2}$
k	Permeability	m^2
l	Length	m
p	Pressure	Pa
q	Source term	-
Q	Rate	$PV \cdot day^{-1}$
S	Saturation	-
t	Time	s
T	Transmissibility	$m \cdot s^{-1} \cdot Pa^{-1}$
u	Velocity	$m \cdot s^{-1}$
x	Mass fraction	-
z	Mole fraction	-
Γ	Cell face	-
μ	Viscosity	Pa·s
π	Interfacial pressure	Pa
ρ	Density	$kg \cdot m^{-3}$
θ	Angle	Degrees
ϕ	Porosity	-
Ω	Cell	-

1

INTRODUCTION

For the first time ever in the Netherlands, energy production from renewable sources surpassed fossil energy production in volume in the first half of 2024. Figure 1.1 visually represents the energy production per source from 2015 to 2024. Renewable energy sources can be categorized into three groups: photovoltaics [20], wind energy [36, 53], and bio-energy [75]. In 2023, 85% of renewable energy in the Netherlands was made up of photovoltaic and wind energy [30]. However, a disadvantage of these energy sources is the fact that they are intermittent of nature, making them uncontrollable. Additionally, renewable energy supply is challenging to predict as weather forecasting remains an active topic of research [48, 74]. To account for these intermittencies and ensure a robust energy system, large-scale energy storage systems are deemed critical.

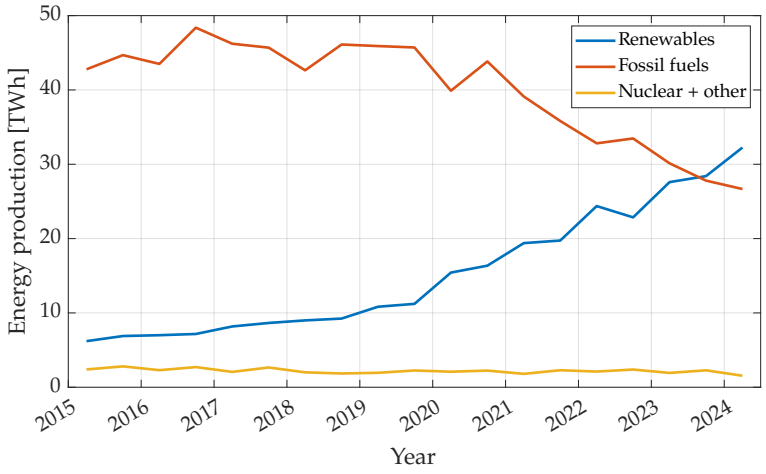

Figure 1.1: Electricity generation per source over time [70].

Large-scale energy storage exists in many forms. For example, energy can be stored using mechanisms such as flywheels [39], or by the use of electrochemicals [15]. Other candidates are thermal [2] and chemical energy storage [62]. Chemical energy storage is suitable for the storage of substantial quantities of energy. In Fig. 1.2, an overview of the energy density and specific energy of various chemical compounds is shown.

1.1. Hydrogen as an energy carrier

With global electricity storage demand estimates for 2030 ranging from 11.9-15.7 TWh [32], the necessity for large-scale energy storage systems is clear. For large-scale energy storage systems, hydrogen is a promising energy carrier. The substance is non-reactive and has a comparatively high energy density of 33.3 kWh·kg^{-1}

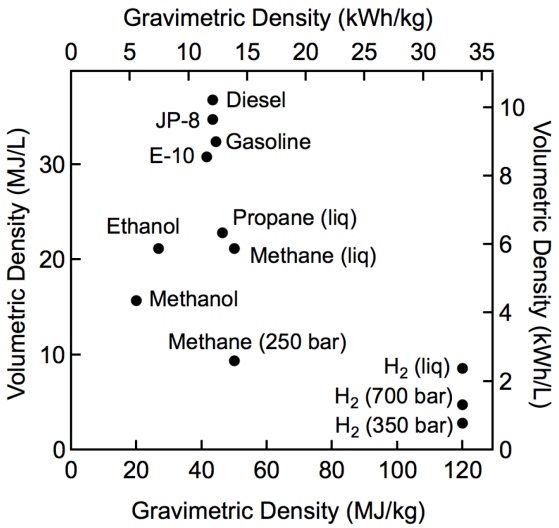

Figure 1.2: Energy density and specific energy for several chemicals, based on Lower Heating Values [77].

[47]. In contrast, large-scale battery technologies such as lithium-ion and sodium-ion report energy densities in the $Wh{\cdot}kg^{-1}$ range [38, 57, 18]. Additionally, hydrogen can be produced using various techniques, of which the two most well-known are steam methane reforming (SMR) [50] and water electrolysis [26]. Figure 1.3 illustrates the share of each production method during the period from 2020-2023, and its outlook for 2030. The following section will elaborate on both production methods.

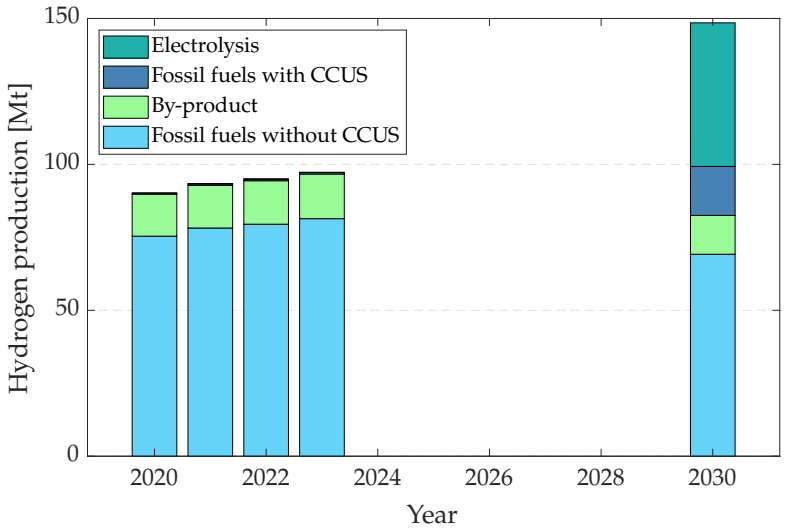

Figure 1.3: Global hydrogen production share for electrolysis, production through fossil fuels with and without Carbon Capture, Utilization and Storage (CCUS), and as byproduct, in the Net Zero Scenario, 2019-2030 [31].

1.1.1. Steam methane reforming

In the SMR method, hydrocarbon base material is catalytically converted into hydrogen and carbon oxides. For the base material, methane (CH_4) is used. A flow diagram for the SMR process is given in Fig. 1.4. The reforming step, described by Eq. (1.1), converts methane and steam into hydrogen and carbon monoxide. Then, the products are fed into the water-gas shift reactor where hydrogen is produced according to Eq. (1.2).

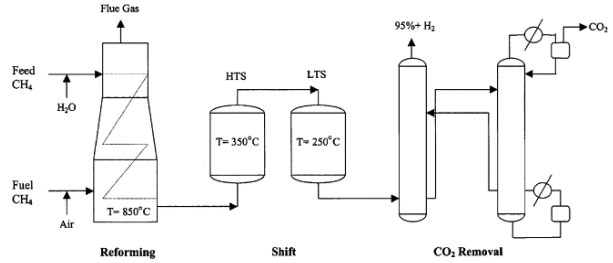

Figure 1.4: Flowchart for SMR process [4].

$$CH_4 + H_2O \leftrightarrow CO + 3H_2 \tag{1.1}$$

$$CO + H_2O \leftrightarrow CO_2 + H_2 \tag{1.2}$$

Finally, CO_2 may be removed from the mixture through amine scrubbing [63] or pressure swing adsorption [68].

1.1.2. Electrolysis

Water electrolysis is an established technique for producing hydrogen. Its working principle is the splitting of water molecules using electrical energy. In an electrolyzer, water is decomposed into hydrogen and oxygen at the cathode and anode:

$$\text{ANODE:} \quad H_2O \rightarrow 2H^+ + \tfrac{1}{2}O_2 + 2e^- \tag{1.3}$$

$$\text{CATHODE:} \quad 2H^+ + 2e^- \rightarrow H_2 \tag{1.4}$$

The overall reaction is formed by combining Eq. (1.3) and Eq. (1.4):

$$H_2O \rightarrow H_2 + \tfrac{1}{2}O_2 \tag{1.5}$$

Various water electrolysis techniques exist, with the main difference being the type of electrolyte used within the cell. Commercially available methods are, for example, alkaline water electrolysis [10], proton exchange membrane cells [66], and solid oxide electrolysis cells [27].

1.2. Hydrogen storage systems

For hydrogen to compensate for seasonal intermittencies in renewable electricity supply, it must be produced and stored when renewable electricity is abundant. When necessary, the hydrogen can be retrieved and converted into electricity using fuel cells [76] for various uses. Hydrogen storage systems can be divided into two categories: surface hydrogen storage and subsurface hydrogen storage. Both categories will be discussed below.

1.2.1. Surface hydrogen storage

Hydrogen may either be stored in liquid form [78], in the form of liquid-organic hydrogen carriers [61], or in solid state [65]. To account for energy storage needs in the TWh range however, these storage methods do not suffice. Besides, they require additional production processes. Another option for hydrogen storage is to make use of geological formations in the subsurface.

1.2.2. Subsurface hydrogen storage

For the large volumes of hydrogen needed for adequate energy storage capacity, subsurface hydrogen storage is required to complement the limited surface storage capacity technologies discussed above. To this end, three promising storage hosts have emerged: salt caverns [12], depleted hydrocarbon reservoirs [52], and aquifers [33]. An overview of these is shown in Fig. 1.5. Each category will be briefly discussed below.

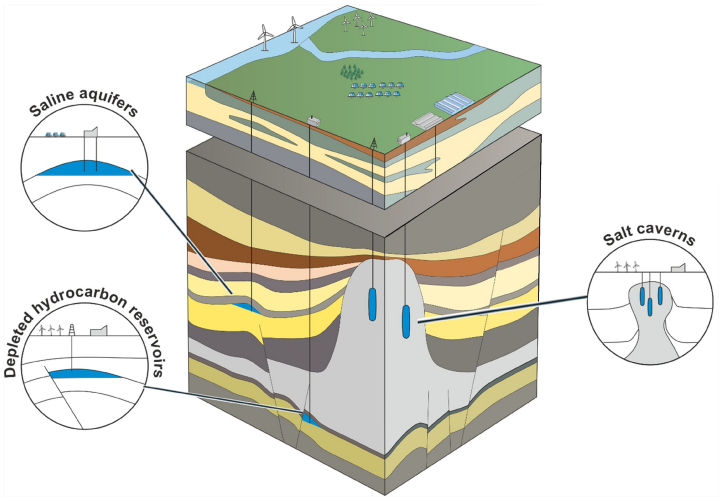

Figure 1.5: Schematic overview of different techniques for subsurface hydrogen storage systems. Adapted from [49].

Salt cavern hydrogen storage

Salt caverns are holes in salt deposits that are produced by the injection of water into the salt rock well. They are the most mature technique listed here, with the first hydrogen storage salt cavern opened in 1972 in Teesside, United Kingdom [72]. An advantageous characteristic of salt caverns is the fact that the salt is low in porosity and permeability, hindering hydrogen dissipation. Additionally, it is inert towards hydrogen. However, since the storage capacity of salt caverns is in the GWh range, the technique is not suitable for large-scale energy storage systems. Additionally, large volumes of fresh water are required for dissolution mining, making the practice less sustainable.

Depleted hydrocarbon reservoir hydrogen storage

Another option for subsurface hydrogen storage is the use of depleted oil and gas reservoirs. In oil and gas reservoirs, hydrocarbons have accumulated over the years in the pore space of rocks. The pore space of the rock is considered the reservoir, and the caprock on top prevents the migration of the hydrocarbon beyond limits. Since these reservoirs have long existed and have been actively exploited over the past century, they are thought to be a feasible storage method. In addition, any residual native gas in the reservoir can be used as cushion gas. Cushion gas serves to pressurize the reservoir, ensuring proper extraction in the case of hydrogen extraction from the depleted reservoir.

Aquifer hydrogen storage

Aquifers are underground porous media that are water-bearing. They offer larger storage capacities compared to salt caverns, and thus present an opportunity for cost-effective large-scale energy storage. However, a lot is still unclear on the geological characteristics of aquifers, and research has to be done to ensure trapping and sealing of hydrogen by the formation [44]. Such trapping mechanisms can be an impermeable caprock and proper surrounding hydrostatic and threshold pressures [23].

1.3. Research objective

In this introduction, the necessity for large-scale energy storage systems has been substantiated. Storage of energy in the form of hydrogen looks to be a promising candidate for the realization of such systems. For the safety and performance necessary, it is essential to be able to model and simulate subsurface hydrogen storage systems. This work, therefore, aims to identify reservoir parameters that affect storage potential and reservoir performance. Additionally, demonstrating the feasibility of hydrogen storage on fieldscale is considered a key objective.

1.4. Thesis outline

The outline of this thesis is as follows: in Chapter 2, an introduction to the concepts of flow in porous media and the equations governing this is given. Then, Chapter 3 elaborates on the Cartesian and corner-point geometry. Chapter 4 describes the process of validation of the corner-point geometry with respect to Cartesian geometry. The reservoir parameter analysis is covered in Chapter 5, after which the field-scale simulations are described in Chapter 6. Finally, a discussion and conclusion are presented in Chapter 7.

2

FLOW IN POROUS MEDIA

The geo-engineering concepts of subsurface hydrogen storage described in Chapter 1 demand a proper understanding of the way in which fluids and gases move in the underground. Additionally, it is of interest how the substance physically interacts with the reservoir itself. Therefore, this chapter will elaborate on the physical parameters and concepts of flow in porous media.

2.1. Physical parameters

This section will briefly introduce a number of physical parameters that govern flow in subsurface reservoirs.

2.1.1. Porosity

Rock porosity, denoted by ϕ, is the fraction of the medium volume that consists of void space, with $0 \leq \phi < 1$. The void space consists of two parts. On one end, the interconnected pore space through which fluid can flow, and on the other end, the disconnected pores that are unavailable to flow. The latter are referred to as dead-ends. For reservoir simulation, only the interconnected pores are of interest. Therefore, it is common to specify these as *effective porosity* [42]. Although porosity usually depends on pressure, it is customary to assume that rock porosity only varies spatially.

2.1.2. Permeability

Permeability, denoted by $\mathbf{K}$, quantifies the rock's ability to transmit a single fluid under specified conditions. Permeability is usually strongly correlated to porosity, since the connection and orientation of the rock pores are crucial for fluid flow. However, permeability is not by definition proportional to porosity. Permeability is defined as the proportionality factor between flow velocity and a potential gradient $\nabla\Phi$ [17]:

$$\vec{u} = -\frac{K}{\mu} \cdot \nabla\Phi \,. \tag{2.1}$$

Here, μ is the fluid viscosity and $\vec{u}$ is the flow velocity. The permeability generally is a full tensor, i.e.

$$\mathbf{K} = \begin{bmatrix} k_{xx} & k_{xy} & k_{xz} \\ k_{yx} & k_{yy} & k_{yz} \\ k_{zx} & k_{zy} & k_{zz} \end{bmatrix} . \tag{2.2}$$

However, usually the coordinate system is aligned with the layering in the reservoir, such that $\mathbf{K}$ is diagonal

[34]:

$$\text{1-D:} \quad \mathbf{K} = k, \quad \text{2-D:} \quad \mathbf{K} = \begin{bmatrix} k_x & 0 \\ 0 & k_y \end{bmatrix}, \quad \text{3-D:} \quad \mathbf{K} = \begin{bmatrix} k_x & 0 & 0 \\ 0 & k_y & 0 \\ 0 & 0 & k_z \end{bmatrix}. \tag{2.3}$$

2.1.3. Relative permeability

Relative permeability, k_r, represents the additional resistance to flow of a phase in the presence of another. It is not directly measurable, but must be experimentally determined or modelled. To this end, several models have been developed, such as the Corey [16] and the Brooks-Corey [11] models. These models relate the relative permeability for both the wetting and the non-wetting phase to their corresponding saturation. In this work, experimentally measured relative permeability curves are used [46]. The relative permeability curves were extended across the full saturation range through numerical history matching with an LET model [43]. The relative pressure curves obtained are shown in Fig. 2.1.

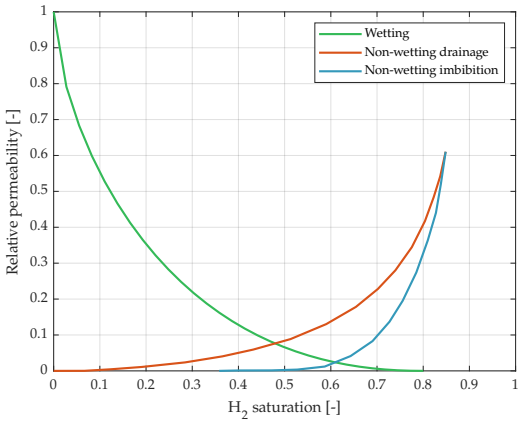

Figure 2.1: Relative permeability curves used for simulations.

2.2. Governing Equations

The definition of the governing equations involved in flow and transport processes in porous media varies, depending on the composition of the fluid in the reservoir. The most basic way to describe the flow in a reservoir is through a single-phase fluid model. To model subsurface hydrogen storage systems, multi-component multiphase flow models are required, which will be covered afterwards.

2.2.1. Single-phase flow

The flow of a single-phase fluid through a porous medium is governed by the mass conservation equation, namely [5]:

$$\frac{\partial(\phi\rho)}{\partial t} + \nabla \cdot (\rho \mathbf{u}) = q. \tag{2.4}$$

In this equation, t is time, ϕ is rock porosity, ρ is fluid density, $\mathbf{u}$ is fluid velocity, and finally, q is the source term. The source term represents, for example, wells. Darcy's law [17, 80] can be used to express the fluid

velocity as:

$$\mathbf{u} = -\frac{\mathbf{K}}{\mu} \cdot (\nabla p - \rho g \nabla z) \, ; \tag{2.5}$$

where $\mathbf{K}$ is the rock permeability tensor, μ is the fluid viscosity, p is the pressure, g is the gravitational constant and z is the spatial coordinate in vertical direction.
Inside the reservoir domain Ω, Eq. (2.4) and Eq. (2.5) are combined to be able to solve for the pressure. Assuming that porosity ϕ and density ρ are constant in time yields the following equation:

$$\nabla \cdot \mathbf{u} = \nabla \cdot \left[-\frac{\mathbf{K}}{\mu} \left(\nabla p + \rho g \nabla z \right) \right] = \frac{q}{\rho} \, . \tag{2.6}$$

Finally, on the reservoir boundary $\partial\Omega$, a no-flow boundary condition is imposed to close the boundary:

$$\mathbf{u} \cdot n = 0, \tag{2.7}$$

where n represents the normal vector on the boundary $\partial\Omega$. This boundary condition ensures an isolated system, in which no fluid exits or enters the reservoir.

2.2.2. Multi-component multiphase flow

In this section, multi-component multiphase flow will be described. In subsurface hydrogen storage simulation models, often a two-component two-phase fluid model is utilized. The mass conservation equation for a system, composed of n_c components, composed of n_{ph} phases reads:

$$\frac{\partial}{\partial t} \left(\phi \sum_{\alpha=1}^{n_{ph}} x_{c\alpha} \rho_\alpha S_\alpha \right) + \nabla \cdot \left(\sum_{\alpha=1}^{n_{ph}} x_{c\alpha} \rho_\alpha \boldsymbol{u}_\alpha \right) - \sum_{\alpha=1}^{n_{ph}} x_{c\alpha} q_\alpha = 0, \quad \forall c \in \{1, \ldots, n_c\} \, ; \tag{2.8}$$

where $x_{c\alpha}$ is the mass fraction of component c in phase α and with Darcy's velocity defined as:

$$\boldsymbol{u}_\alpha = -\frac{\mathbf{K} k_{r\alpha}}{\mu_\alpha} \left(\nabla p_\alpha - \rho_\alpha g \nabla z \right) \, . \tag{2.9}$$

In this equation, $k_{r\alpha}$ is the phase relative permeability [1] and p_α is the pressure in phase α. In this case, $\alpha \in (w, \, n)$ with w and n denoting the wetting and non-wetting phase, respectively. The phase pressures p_α can be related through the capillary pressure:

$$p_c = p_n - p_w \, . \tag{2.10}$$

Furthermore, the following constraint holds for the saturation:

$$\sum_{\alpha=1}^{n_{ph}} S_\alpha = 1 \, . \tag{2.11}$$

This system of non-linear differential equations is then solved under no-flow boundary conditions using implicit temporal discretization and finite-volume spatial discretization [51]. The variables for which the system is solved are the wetting phase pressure p_w and the total mole fraction of the primary component z_c, i.e., $c = \mathrm{H}_2$. The mole fraction z_c is expressed as:

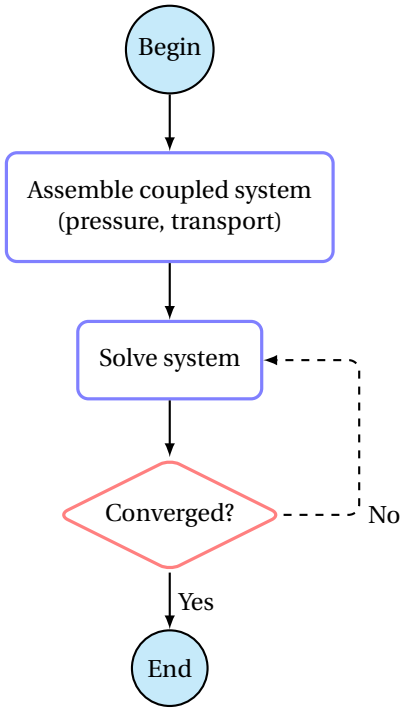

Figure 2.2: Overview of coupled FIM scheme.

$$z_c = \sum_a \frac{x_{c,a}\rho_a S_a}{\sum_a \rho_a S_a} \,. \tag{2.12}$$

For linearization, the Newton-Raphson method [45, 22] is employed. This method is capable of robustly handling the non-linearities present in the governing equations.

2.3. Solution methods

Since the above-described non-linear system of equations does not have a general analytical solution, it is numerically solved instead. As stated before, a finite-volume spatial discretization is employed as it ensures mass conservation. For numerically modelling the multiphase flow system, the Fully Implicit Method (FIM) is adopted.

2.3.1. Fully Implicit Method

In the coupled FIM solution strategy, flow (pressure) variables and transport (mole fraction) variables are coupled into a single system. The combined system of nonlinear equations is then solved by using Newton-Raphson iterations. Unlike sequential fully implicit schemes [35], the near-elliptic pressure equation and the near-hyperbolic transport equation are solved simultaneously. This ensures strong coupling between flow and transport phenomena, in effect improving robustness and stability [3, 8]. In Fig. 2.2, a flow diagram of the coupled FIM is shown.

2.3.2. Newton-Raphson method

The Newton-Raphson method (NRM) for linearization is a technique that is employed for sequentially approximating the zeros of a real-valued function:

$$f(x) = 0\,. \tag{2.13}$$

The general relation of the NRM in a univariate case is the following:

$$x_{n+1} = x_n - \frac{f(x_n)}{f'(x_n)}, \quad n = 0, 1, 2, \dots\,; \tag{2.14}$$

where f and f' represent the objective function and its first derivative, respectively. The number of iterations is denoted by n. x_0 is the initial guess, and x_1 is obtained by substituting x_0 in Eq. (2.14). A visual overview of the process is given in Fig. 2.3. This process is continued iteratively, with x_n being derived using x_{n-1}, until a predefined criterion ϵ is met, i.e., until:

$$|x_{n+1} - x_n| < \epsilon\,; \tag{2.15}$$

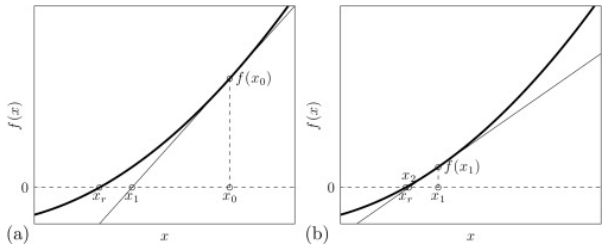

Figure 2.3: A visualization of the Newton-Raphson method. a) First iteration, resulting in point x_1 from tangent line at $(x_0, f(x_0))$ and b) second iteration leading to point x_2 from tangent line at $(x_1, f(x_1))$ [24].

3

GRID DISCRETIZATION

This chapter will cover the grid discretization methods that have been employed in this work. This is a relevant characteristic, since the Finite Volume Method (FVM) is the numerical scheme that is used.

3.1. Finite Volume Method

The Finite Volume Method is a numerical modelling approach that serves to convert the partial differential equations (PDEs) governing fluid flow from differential volumes into discrete algebraic equations. These equations are defined over so-called finite volumes [51]. These finite volumes represent cells or elements. Crucial to the process is discretizing the geometric domain into finite volumes. In the case of FVM, this entails discretizing the domain into non-overlapping cells. Discretization of the grid domain can be categorized into two main domains: structured and unstructured discretization. Subsequently, the structured grid discretization method domain can be divided into two methods that will be discussed below: Cartesian geometry (CG) discretization and corner-point geometry (CPG) discretization.

3.2. Cartesian geometry

A Cartesian grid is the simplest form of a structured grid. It consists of unit squares in two dimensions, and of unit cubes in three dimensions. This results in a grid in which all of the vertices are integer points. The general definition is as such: a Cartesian grid consists of congruent rectangles in 2D and of rectilinear parallelepipeds in 3D [42]. Cartesian grids are simple to implement and have straightforward indexing. They work well for domains with simple geometries. However, the Cartesian gridding scheme makes it unsuitable for complex and irregular reservoirs. Moreover, it requires many cells to approximate non-rectangular domains. Figure 3.1 provides a visual representation of a rectangular Cartesian grid domain.

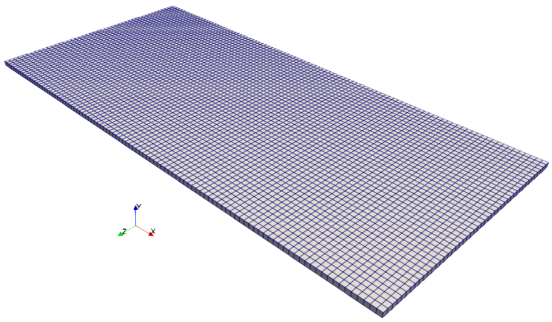

Figure 3.1: Visual representation of a 220 × 60 × 1 Cartesian grid.

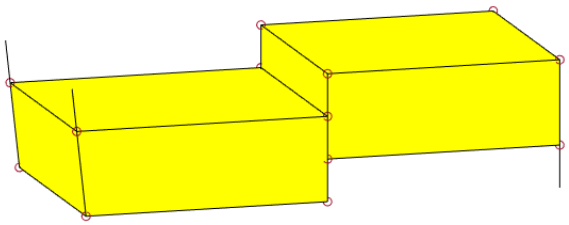

Figure 3.2: Illustration of two corner-point grid cells, each restricted by four pillars, and by two corner-points per pillar.

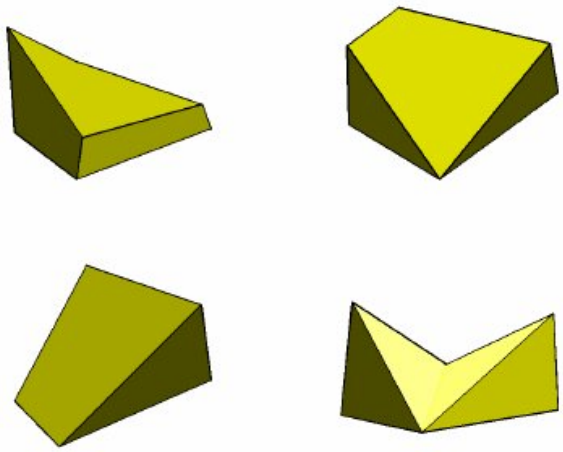

Figure 3.3: Deformed cells in corner-point grid models.

3.3. Corner-point geometry

In order to be able to model more complex and realistic geological structures, the corner-point geometry is introduced [59]. In corner-point geometry, a set of hexahedral cells is aligned in a Cartesian manner. This way, each cell can be identified using ijk indexing. In essence, a corner-point grid is made up of a set of vertical/inclined pillars over a Cartesian 2D mesh. Each cell has eight corner points, confined by four pillars. Each pillar hosts two corner points for every adjacent cell, see Fig. 3.2. The grid consists of $n_x \times n_y \times n_z$ cells, with the i-index cycling first, then the j-index, and finally the k-index. The k-index is defined as the negative z-direction.

Up until this point, the geometry of a corner-point grid has not differed much from that of a regular Cartesian grid. However, in order to model geological features like erosion and pinch-outs, the corner-point method allows for the collapse of points along its pillar. This allows for irregular and degenerate cells that can have fewer than six faces. Figure 3.3 shows four examples of such degenerate cells.

To illustrate the introduced method, the construction of a faulted $2 \times 2 \times 2$ corner-point grid is shown in Fig. 3.4. For an $n_x \times n_y \times n_z$ grid, the number of pillars is equal to $(n_x + 1) \times (n_y + 1)$. Individually, every pillar is defined by the x y z coordinates of its endpoints.

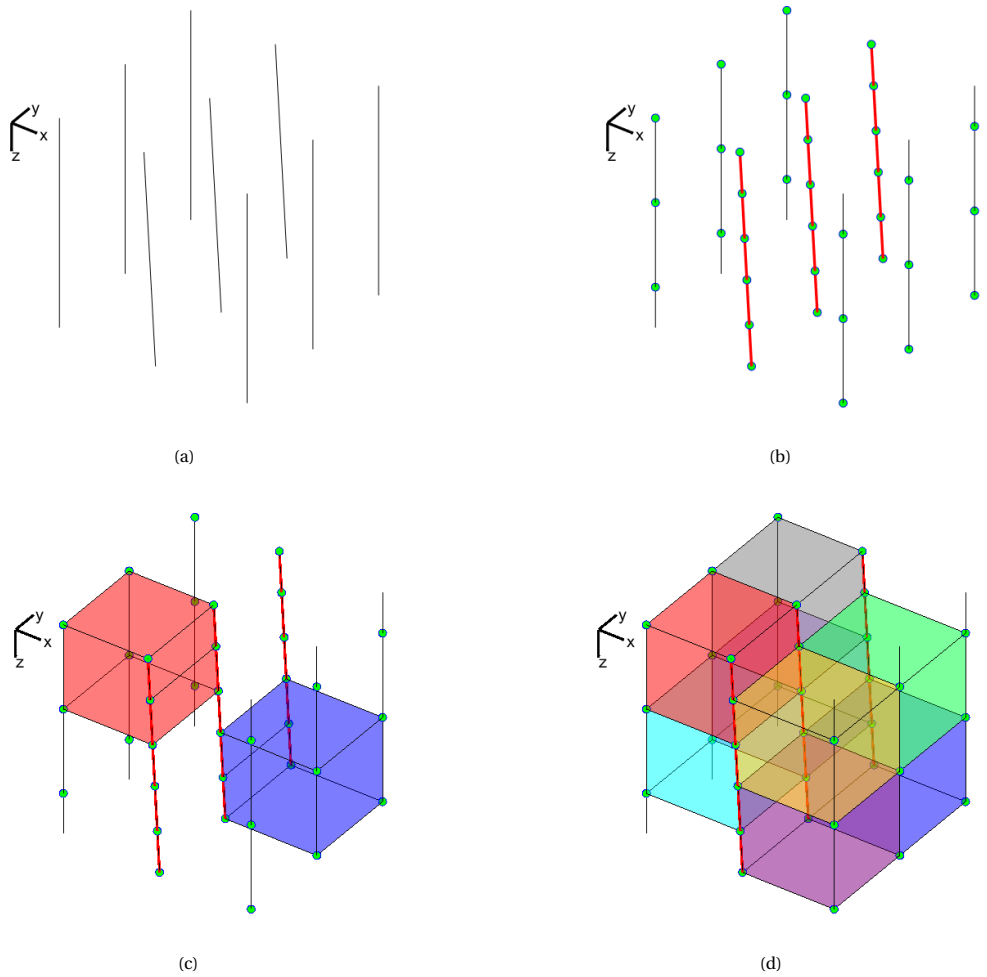

Figure 3.4: Illustration of the construction of a corner-point grid. First, the pillars are constructed (a), on which corner points are placed (b). The pillars that are faulted are marked red. Each cell is defined by the location of eight corner points on four pillars (c). Finally, the full $2 \times 2 \times 2$ grid is constructed [42].

3.3.1. Computing geometry

Whereas for Cartesian grids, it is straightforward to compute cell centroids, volumes, face areas, and normals, this is not the case for complex grid structures, such as corner-point grids. This section will cover the computation of the geometry of corner-point grid cells. For every cell, the input file provides cell vertices and faces, see Fig. 3.5a. A single face is then considered, defined by the points $\vec{p}(i_1), ..., \vec{p}(i_m)$. Additionally, $\alpha = (\alpha_1, ..., \alpha_m)$ denotes an index describing how points $\vec{p}(i_1), ..., \vec{p}(i_m)$ are connected to form the perimeter of a face. In Fig. 3.5a, face 2 consists of points $\vec{p}(2)$, $\vec{p}(4)$, $\vec{p}(6)$ and $\vec{p}(8)$, with $\alpha = (2, 4, 6, 8)$. For every surface, the interpretation of the surface spanned by its nodes has to be chosen. Therefore, the *hinge point* is employed. The hinge point is computed as such:

$$\vec{p}_h = \sum_{k=1}^{m} \frac{\vec{p}(\alpha_k)}{m} \; ; \tag{3.1}$$

where m is the number of points that make up the face. Now the hinge point allows for tesselation of the face into m triangles, which is shown in Fig. 3.5b. Each of these triangles is defined by the points $\vec{p}(\alpha_k)$, $\vec{p}(\alpha_{mod(k,m)+1})$, and $\vec{p}_h$ for $k = 1, .., m$. The triangles have center point $\vec{p}_c^{\,k}$ defined as the average

of its vertices and a normal vector given as:

$$\vec{n}^k = \left(\vec{p}\left(\alpha_{\bmod(k,m)+1}\right) - \vec{p}\left(\alpha_k\right)\right) \times \left(\vec{p}_h - \vec{p}\left(\alpha_k\right)\right) = \vec{v}_1^k \times \vec{v}_2^k \,. \tag{3.2}$$

Its surface area is calculated as:

$$A^k = \sqrt{\vec{n}^k \cdot \vec{n}^k} \,. \tag{3.3}$$

Using the center points $\vec{p}_c^k$, normals $\vec{n}^k$, and surface areas A^k, the total face area, centroid, and normal can be calculated as:

$$A_f = \sum_{k=1}^{m} A^k \,, \tag{3.4a}$$

$$\vec{c}_f = \left(A_f\right)^{-1} \sum_{k=1}^{m} \vec{p}_c^k A^k \,, \tag{3.4b}$$

$$\vec{n}_f = \sum_{k=1}^{m} \vec{n}^k \,. \tag{3.4c}$$

The face centroid and normal resulting from these calculations are shown in Fig. 3.5c. It should be noted that unless the face is square, the centroid does not line up with the hinge point $\vec{p}_h$.
For the computation of the cell centroid, the average of the face centroids is taken:

$$\vec{c}_c = \sum_{k=1}^{m_f} \frac{\vec{c}_f}{m_f} \,, \tag{3.5}$$

where m_f is the number of faces. The cell volume is then triangulated by connecting the cell centroid $\vec{c}_c$ to the face triangles, see Fig. 3.5d. The vector $\vec{c}_r^k = \vec{p}_c^k - \vec{c}_c$ is then defined for every tetrahedron, and its volume is calculated:

$$V^k = \frac{1}{3} \vec{c}_r^k \cdot \vec{n}^k \,. \tag{3.6}$$

Finally, the cell volume and its centroid are defined as follows:

$$V = \sum_{k=1}^{m_t} V^k \,, \tag{3.7}$$

$$\vec{c} = \vec{c}_c + \frac{3}{4V} \sum_{k=1}^{m_L} V^k \vec{c}_r^k \,. \tag{3.8}$$

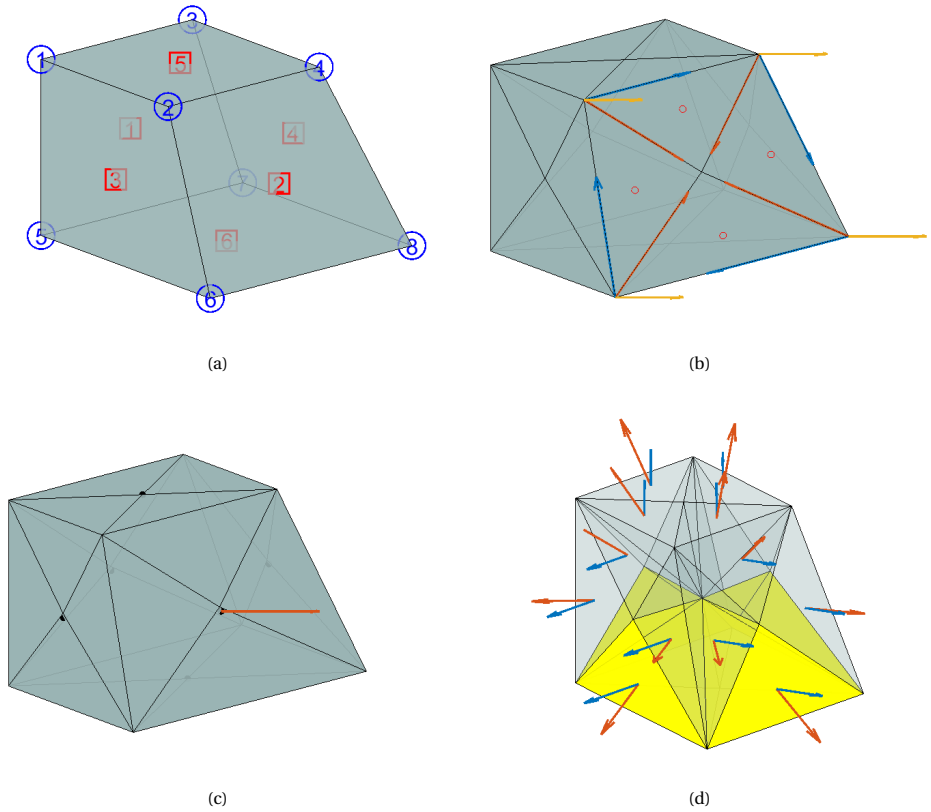

(a) (b)

(c) (d)

Figure 3.5: Illustration of computation of geometry for a CPG cell. (a) The cell with its face numbers (red) and node (blue) numbers. (b) Tesselation of faces with vectors $\vec{v}_1^k$ (blue), $\vec{v}_2^k$ (red), and $\vec{n}^k$ (orange). (c) Face centroids and normal vector of face 2 computed from tesselation. (d) Triangulation of the cell volume with vectors $\vec{n}^k$ (green) and $\vec{c}_r^k$ (red) [42].

3.3.2. Two-point flux approximation

In Section 3.3, it has been discussed that cells in corner-point format may have irregularly shaped faces. Furthermore, in corner-point grid models, it is possible for cells to have more neighbouring cells than the usual six in Cartesian grids. Figure 3.6 shows two cells and its neighbours in the Johansen formation with six and eight neighbours. For this reason, it is important to have a proper definition of the flux that is exchanged between two neighbouring cells.

(a) (b)

Figure 3.6: Cells in Johansen formation with (a) six neighbours and (b) eight neighbours.

For finite volume discrete systems, Darcy's velocity (Eq. (2.9)) can be rewritten in integral form, on a discrete cell Ω_i as follows:

$$\int_{\partial\Omega_i} \vec{u}\cdot\vec{n}dS = -\int_{\Omega_i} q\; d\vec{x}\,. \tag{3.9}$$

Next, the flux over the two adjacent cells *i* and *j* is expressed as such:

$$u_{i,k} = \int_{\Gamma_{i,k}} \vec{u}\cdot\vec{n}dS\,. \tag{3.10}$$

The cell faces $\Gamma_{i,k}$ are referred to as half-faces [9], since they are associated with a grid cell Ω_i and outward-pointing vector $\vec{n}_{i,k}$. An assumption here is that the grid matches, meaning that each half face $\Gamma_{i,k}$ has a twin half face $\Gamma_{k,i}$ with face areas $A_{k,i} = A_{i,k}$ and normal vector $\vec{n}_{k,i} = -\vec{n}_{i,k}$. Now, the integral over the cell face can be approximated by the midpoint rule:

$$u_{i,k} \approx A_{i,k}(\mathbf{K}\nabla p)\left(\vec{x}_{i,k}\right)\cdot\vec{n}_{i,k}\,; \tag{3.11}$$

with $\vec{x}_{i,k}$ indicating the centroid of $\Gamma_{i,k}$. The pressure gradient can now be determined using the one-sided finite difference. It is defined as the difference between the pressure $\pi_{i,k}$ at the face centroid and the pressure at a point inside the cell. The value of the pressure at the cell center is equal to the average pressure p_i inside the cell, leading to:

$$u_{i,k} \approx A_{i,k}\mathbf{K_i}\frac{\left(p_i-\pi_{i,k}\right)\vec{c}_{k,i}}{\left|\vec{c}_{k,i}\right|^2}\cdot\vec{n}_{i,k} \Rightarrow u_{i,k} \approx T_{i,k}\left(p_i-\pi_{i,k}\right)\,. \tag{3.12}$$

Vectors $\vec{c}_{k,i}$ are defined from the cell centroid to the face centroid. Additionally, the length of the face normals is assumed to be equal to the corresponding face areas $A_{i,k}\cdot\vec{n}_{i,k}$. For the transmissibility, this yields:

$$T_{i,k} = A_{i,k}\mathbf{K_i}\frac{\vec{c}_{k,i}\cdot\vec{n}_{i,k}}{\left|\vec{c}_{k,i}\right|^2}\,. \tag{3.13}$$

The transmissibilities $T_{i,k}$ are named half-transmissibilities, since they are associated with a half face [9]. They are related to a single cell, providing a two-point relation between the flux across a cell face and the pressure difference between the cell and face centroids. Figure 3.7 provides a graphical overview of the two-point flux approximation.

Next, the continuity of face pressure and flux across faces is set:

$$u_{i,k} = -u_{k,i}\,, \tag{3.14a}$$

$$\pi_{i,k} = \pi_{k,i} = \pi_{ik}\,. \tag{3.14b}$$

This then yields:

$$T_{i,k}^{-1}u_{ik} = p_i - \pi_{ik}\,, \tag{3.15a}$$

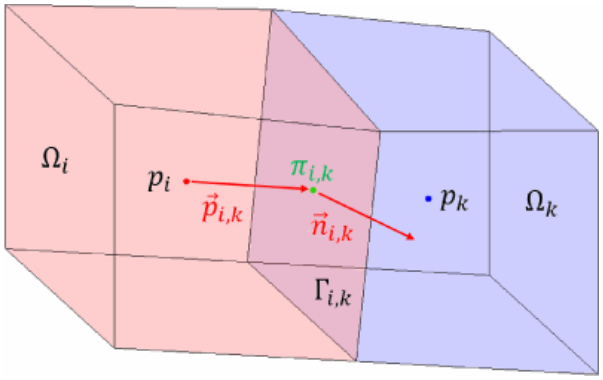

Figure 3.7: Illustration of two-point flux approximation on polyhedral cells [29].

$$-T_{k,i}^{-1}u_{ik} = p_k - \pi_{ik}. \tag{3.15b}$$

Finally, the interface pressure π_{ik} is eliminated, leaving the two-point flux approximation (TPFA) scheme defined as:

$$u_{ik} = \left[T_{i,k}^{-1} + T_{k,i}^{-1}\right]^{-1}\left(p_i - p_k\right) = T_{ik}\left(p_i - p_k\right), \tag{3.16}$$

where T_{ik} represents the combined transmissibility between the two cells. The flux gets effectively approximated across the interface $\Gamma_{i,k}$ between cells Ω_i and Ω_k.

4

VALIDATION

In this chapter, the validation process of CPG discretization with respect to CG discretization will be discussed. The CG method is considered the benchmark in this case, since it is the most straightforward method of grid discretization. The validation process will be performed based on two test cases in 3D, which will be discussed below. Afterwards, the results will be jointly discussed in Section 4.3.

4.1. Test case 1

For the first test case, a homogeneous rectangular box is considered. The reservoir dimensions and other relevant properties are listed in Table 4.1. In Table 4.2, the properties of the 2-component system are described. Using `MRST` [42], a `GRDECL` [56] file is generated. In this file, the `COORD` and `ZCORN` keywords represent the pillar endpoint coordinates and corner point coordinates, respectively. The reservoir simulator is then adjusted accordingly to simulate a reservoir, discretized using CPG. The simulation will be run under monotonous injection, for a period of $t = 150$ days. The well placement is depicted in Fig. 4.1.

Table 4.1: Overview of reservoir properties for validation test 1.

PARAMETER	VALUE	UNIT
l_x	220	m
l_y	60	m
l_z	5	m
n_x	220	-
n_y	60	-
n_z	5	-
ϕ	0.2	-
k_h	1000	mD
k_v/k_h	1	-
Q_{inj}	$1.0 \cdot 10^{-4}$	PV·day^{-1}
P_{prod}	$1.01 \cdot 10^{7}$	Pa
$P_{0,res}$	$1 \cdot 10^{7}$	Pa
T_{res}	300	K
θ_{res}	0	degrees

The placement of the injection and production well relative to the reservoir is depicted in Fig. 4.1

4.2. Test case 2

For the second test case, another rectangular box-shaped reservoir has been considered. Heterogeneity is regarded as a crucial parameter affecting reservoir performance. For this reason, the highly heterogeneous

Table 4.2: Overview of component properties.

PARAMETER	VALUE	UNIT
ρ_{H_2}	1.98	kg·m^{-3}
ρ_{brine}	1060	kg·m^{-3}
μ_{H_2}	$0.965 \cdot 10^{-5}$	Pa·s
μ_{brine}	$5.5 \cdot 10^{-4}$	Pa·s
$c_{w,brine}$	$4 \cdot 10^{-10}$	Pa^{-1}

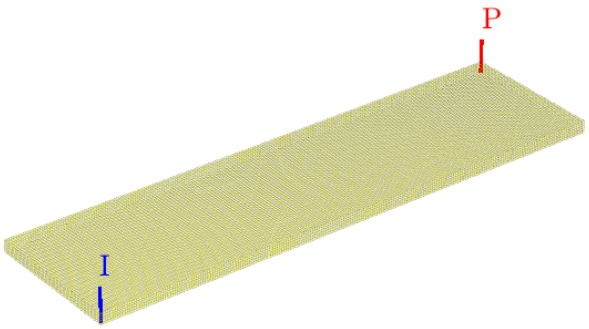

Figure 4.1: Well placement for the validation tests. I and P represent the injection and production wells, respectively.

permeability field of the SPE10 benchmark test [69] is employed for this validation test.
Originally, the 10th SPE Comparative Solution Project was proposed as a benchmark for upscaling methods [69]. It consists of $220 \times 60 \times 85$ (1 122 000) cells, divided into two distinct formations. The top 35 layers represent a shallow-marine Tarbert formation [7], whereas the bottom 50 layers represent a fluvial Upper-Ness formation [6]. Fig. 4.2 shows the horizontal and vertical permeabilities of the model. The distinction between the two formations is clearly visible.

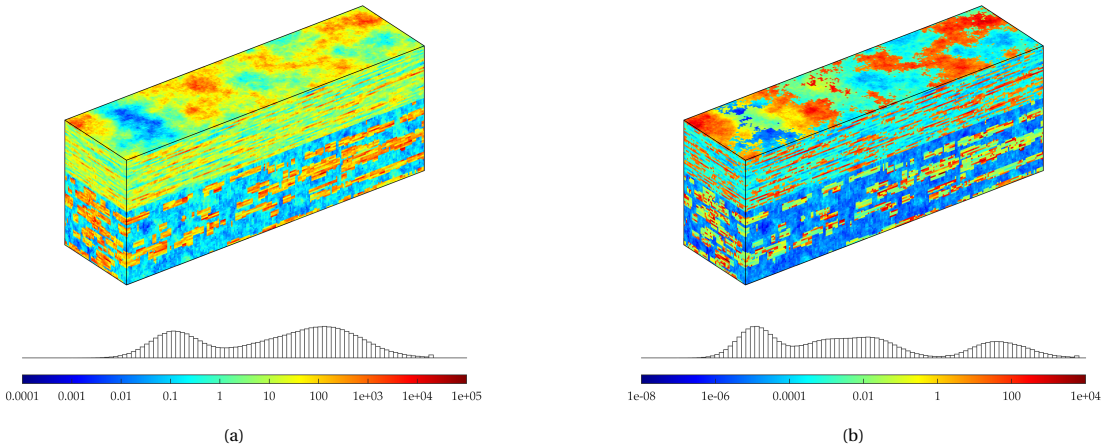

(a) (b)

Figure 4.2: Illustration of (a) horizontal and (b) vertical permeability and its distribution of the SPE10 benchmark test. Permeability is displayed logarithmically, in mD.

The dataset of this project has been widely utilized for comparing various computational methods. For the purpose of this validation test, the model has been employed for its high permeability heterogeneity. This way, it can be identified if CPG discretization leads to different simulation solutions when compared to CG discretization. Because of the highly heterogeneous nature of the model, it would be very computationally demanding to simulate the entire reservoir. For that reason, only the top 5 layers of the Tarbert formation have been selected for the simulation. The horizontal and vertical permeabilities of the top 5 layers are shown in Fig. 4.3,

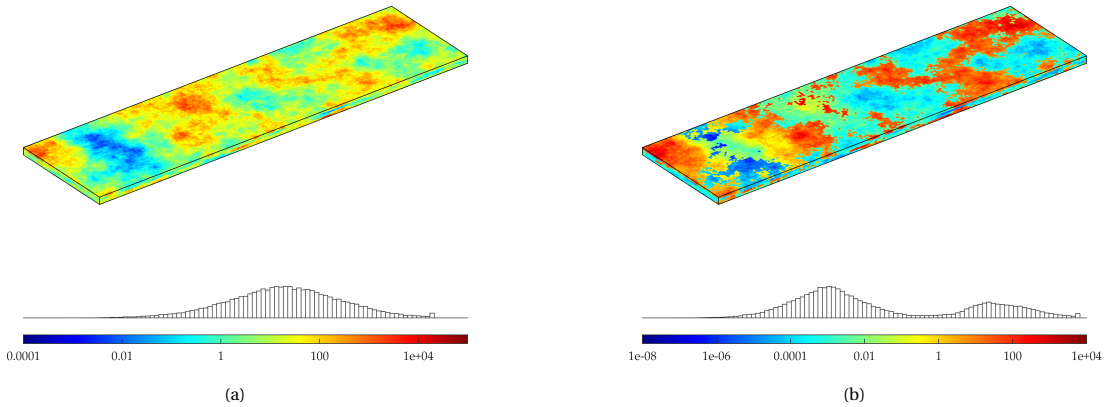

Figure 4.3: Illustration of (a) horizontal and (b) vertical permeability and its distribution of the top 5 layers of the SPE10 benchmark test. Permeability is displayed logarithmically, in mD.

4.3. Results

In this section, the results for both test cases are discussed.

4.3.1. Test case 1

Here, the results are compared for three parameters, namely pressure, saturation, and mass fraction of component 1 in phase 2. For the H_2-brine system used here, that refers to the mass fraction of hydrogen in the liquid phase. In Fig. 4.4 and Fig. 4.5, the simulation solutions for saturation and pressure are shown.

To be certain that there exist no discrepancies between the CG and CPG solution, the pressure, saturation, and mass fraction of component 1 in phase 2 are plotted. This is done for 4 points of interest (POIs). Point 1 is chosen to be the top cell of the well, point 2 is the middle of the reservoir, and points 3 and 4 are arbitrarily chosen cells on the saturation front. An overview of the 4 POIs is provided in Fig. 4.6

The results for each of the four POIs are graphically presented in Fig. 4.7.

4.3.2. Testcase 2

Again, for four POIs, the pressure, saturation, and mass fraction of hydrogen in the liquid phase are graphed. The first two POIs represent the top cell of the well and the top-middle cell. The third POI is chosen near the low-perm zone on the left of the model, and the fourth one at the right side, near the saturation front. An overview of the POIs is given in Fig. 4.10.

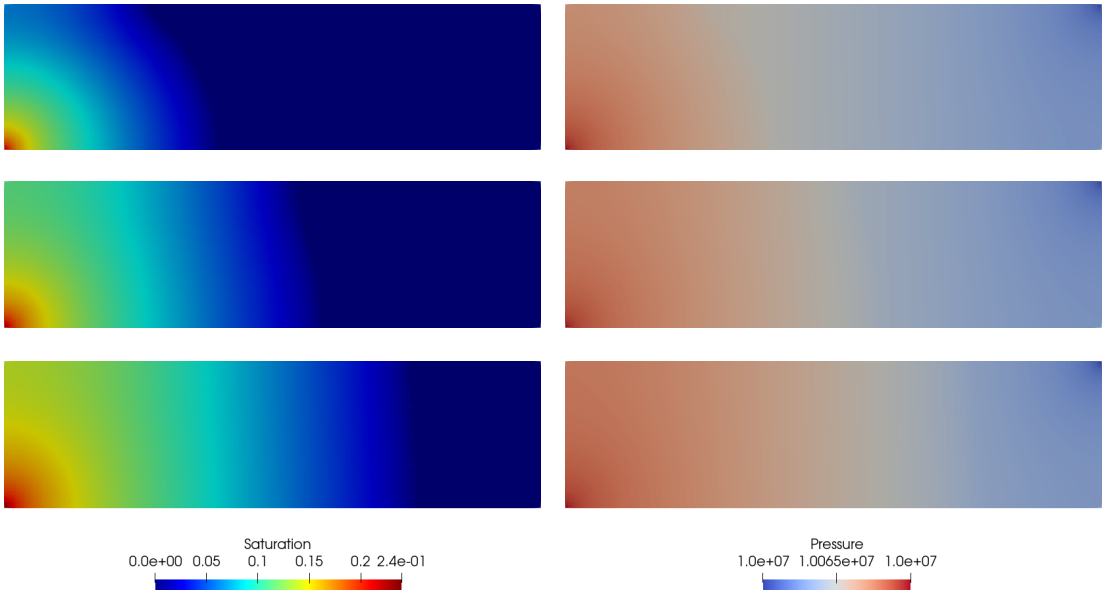

(a) (b)

Figure 4.4: Simulation results for (a) hydrogen saturation and (b) hydrogen pressure at $t = 50,\ 100$ and 150 days for test case 1. These results are from the simulation using CG.

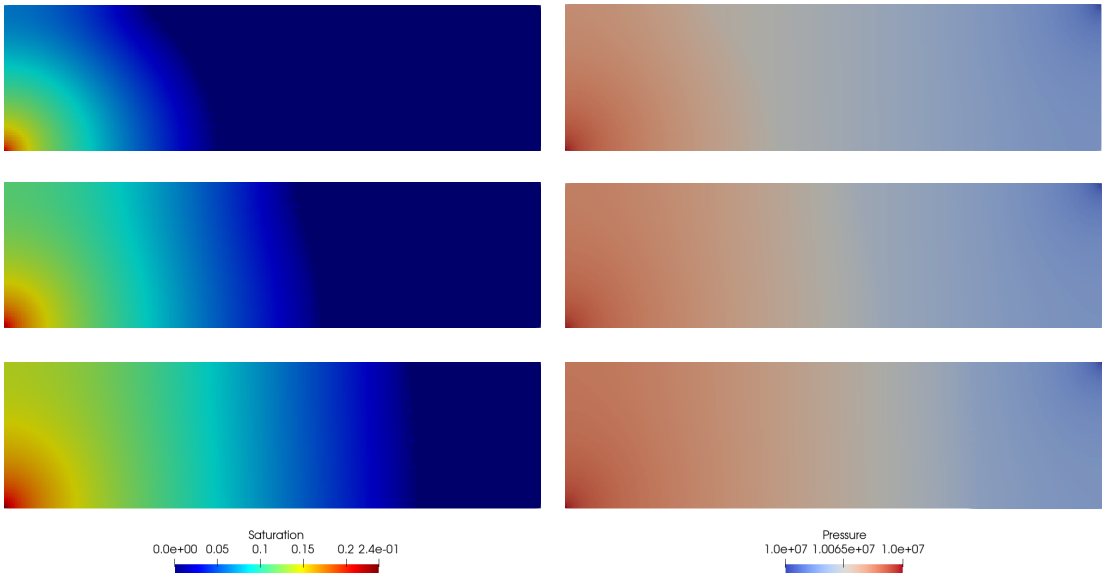

(a) (b)

Figure 4.5: Simulation results for (a) hydrogen saturation and (b) hydrogen pressure at $t = 50,\ 100$ and 150 days for test case 1. These results are from the simulation using CPG.

Figure 4.6: Overview of the POIs for testcase 1.

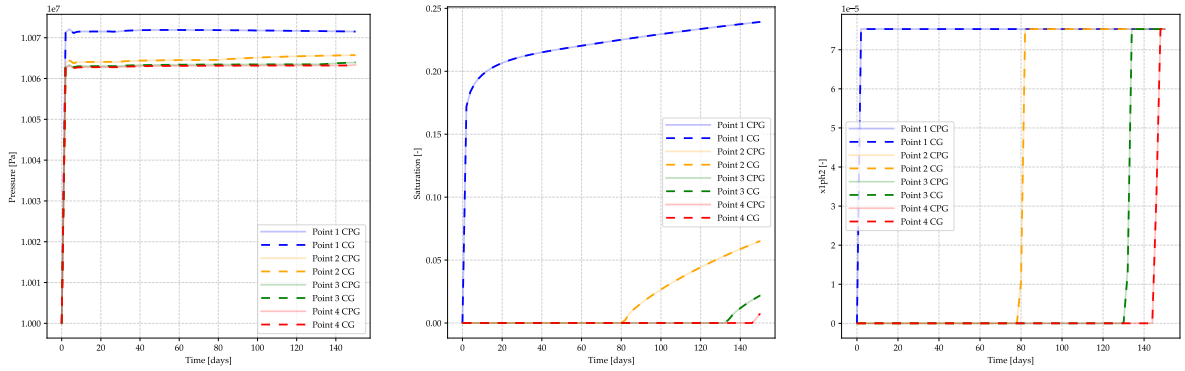

(a) (b) (c)

Figure 4.7: Simulation results for (a) pressure, (b) saturation, and (c) mass fraction liquid hydrogen for testcase 1, for both CG and CPG simulations.

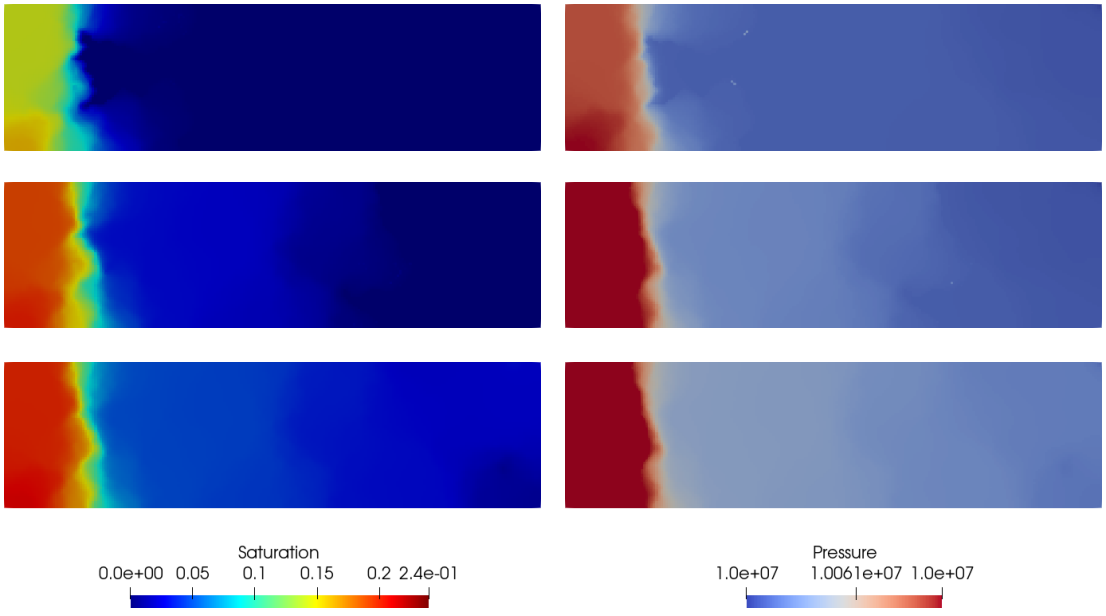

(a) (b)

Figure 4.8: Simulation results for (a) hydrogen saturation and (b) hydrogen pressure at $t = 50,\ 100$ and 150 days for test case 2. These results are from the simulation using CG.

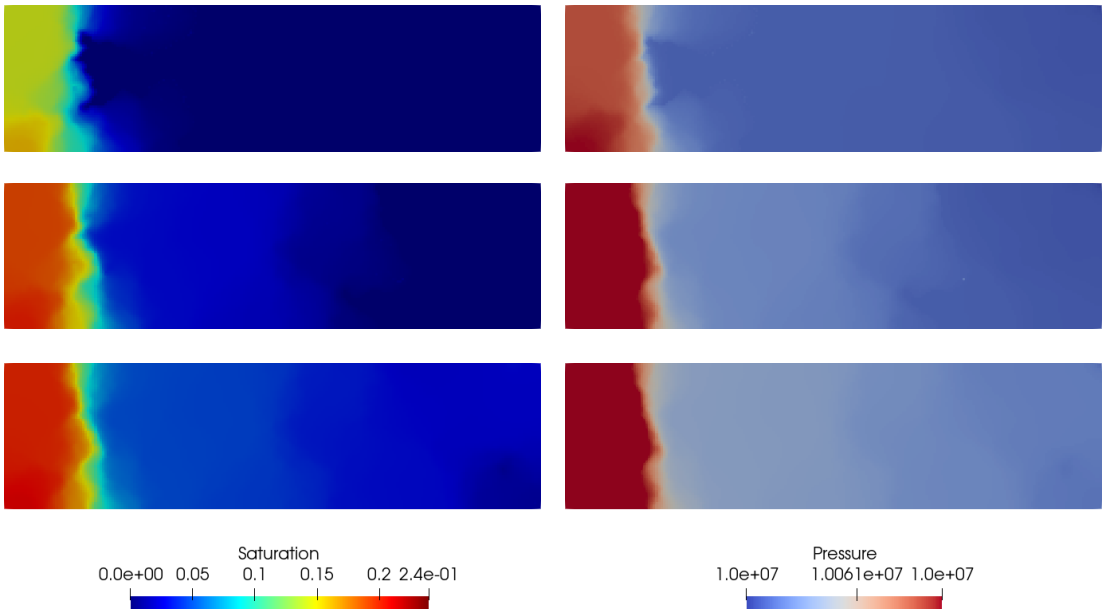

(a) (b)

Figure 4.9: Simulation results for (a) hydrogen saturation and (b) hydrogen pressure at $t = 50,\ 100$ and 150 days for test case 2. These results are from the simulation using CPG.

Figure 4.10: Overview of POI placement for SPE10 benchmark validation test.

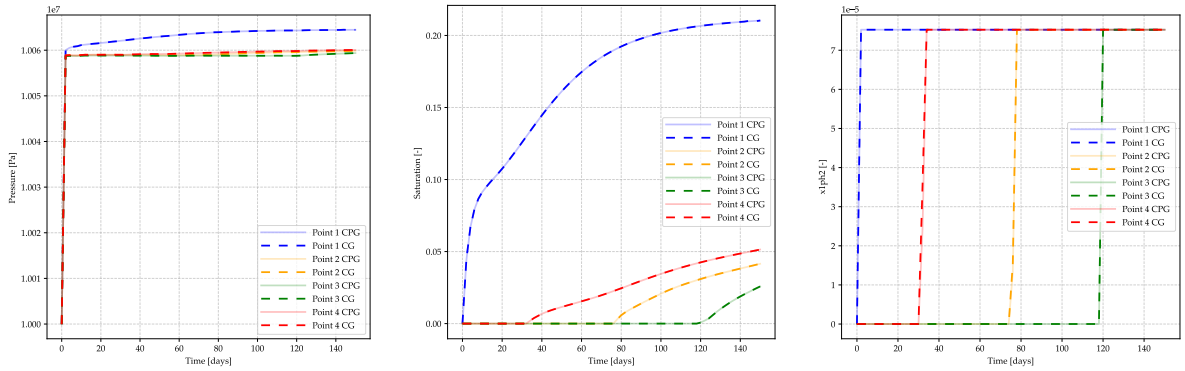

(a) (b) (c)

Figure 4.11: Simulation results for (a) pressure, (b) saturation, and (c) mass fraction liquid hydrogen for test case 2, for both CG and CPG simulations.

5

RESERVOIR PERFORMANCE SENSITIVITY ANALYSIS

This chapter will describe the process of analyzing the sensitivity of reservoir performance to various reservoir parameters. For the purpose of the sensitivity analysis, another test case has been created, upon which various alterations will be made. Afterwards, the results will be compared and discussed.

5.1. Test case reservoir

The test case reservoir has again been synthesized using `MRST` [42]. For hydrogen storage purposes, a reservoir must guarantee the confinement of the injected hydrogen. Therefore, an anticline reservoir has been generated. This will cause the buoyant hydrogen to be confined, enhancing recoverability. The reservoir has been modelled to measure $100 \times 100 \times 20$ meters and is discretized into a $51 \times 51 \times 21$ grid. Table 5.1 presents an overview of relevant reservoir parameters. Figure 5.1 provides a visual representation of the reservoir. For an overview of the component properties, see Table 4.2.

Table 5.1: Overview of reservoir properties.

PARAMETER	VALUE	UNIT
l_x	100	m
l_y	100	m
l_z	20	m
n_x	51	-
n_y	51	-
n_z	21	-
ϕ	0.2	-
k_h	100	mD
k_v/k_h	0.1	-
Q_{inj}	$1.29 \cdot 10^{-8}$	PV·day^{-1}
Q_{prod}	$1.29 \cdot 10^{-6}$	PV·day^{-1}
$P_{0,res}$	$1 \cdot 10^{7}$	Pa
T_{res}	323	K
$\theta_{anticline}$	25	degrees

The total operation time of the reservoir simulation is set to 5 years. A cyclic injection and production scheme will be employed, as follows: three months of injection and production are alternated, separated by an idle time of 3 months. A visual overview of the scheme is provided in Fig. 5.2a. For both injection and production, the same well is used. It is located in the middle of the reservoir and penetrates only the top cell. Figure 5.2b illustrates the well placement.

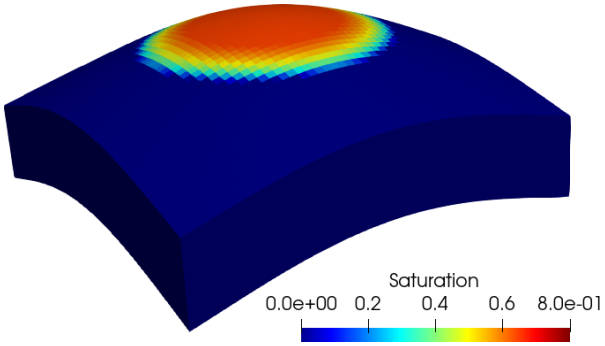

Figure 5.1: Illustration of the base test case, showing hydrogen saturation at $t = 900$ days.

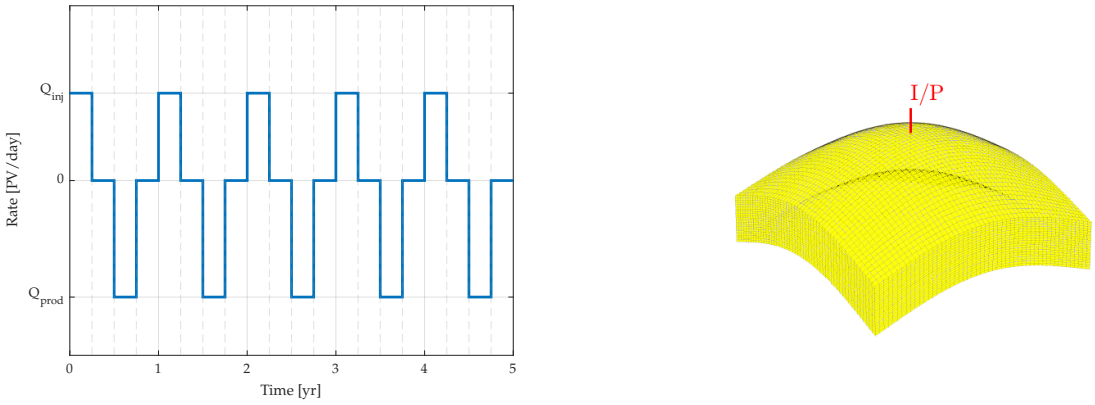

(a) (b)

Figure 5.2: Overview of (a) cyclic scheme and (b) well placement in domed reservoir.

5.2. Parameters

This section will discuss the parameters that have been studied in this sensitivity analysis. The reservoir is analyzed based on the following parameters:

- Porosity
- Permeability
- Anisotropy
- Heterogeneity
- Relative permeability
- Anticline
- Cushion gas

Below, each parameter will be briefly discussed.

5.2.1. Porosity

The reservoir performance is analyzed for various values of porosity. As different reservoir types usually have different values, here the impact of porosity on reservoir performance is analyzed. For the two test cases, porosity has been assigned values of 0.1 and 0.3, respectively.

5.2.2. Permeability

As discussed in Chapter 2, permeability is a fundamental property of the reservoir that quantifies the ability to transmit fluids. It is for this reason that the reservoir performance is tested on this parameter. The values that will be used for permeability are one order of magnitude larger and smaller than that of the base case, i.e., 10 and 1000 mD.

5.2.3. Anisotropy

Subsurface reservoirs often are anisotropic, meaning their properties differ with direction. Anisotropy may have many causes, such as depositional layering of the host rock. Here, anisotropy is defined as the ratio of vertical to horizontal permeability (k_v/k_h). A low degree of anisotropy may restrict vertical migration of the hydrogen and cause it to migrate laterally. This, in effect, can harm recoverability. Therefore, permeability anisotropy is an important parameter to consider. In the base case, the anisotropy degree is set at 0.1. For the two test cases, values of 0.5 and 1.0 will be assigned to the anisotropy. The second test case is thus isotropic.

5.2.4. Heterogeneity

Reservoir heterogeneity plays a significant role in determining the efficiency of subsurface fluid flow [28]. Consequently, it impacts the overall performance of waterflooding and gas injection strategies. Heterogeneity is defined as the spatial variability in reservoir properties, such as permeability and porosity. These variations may create preferential flow paths and impact recoverability.
For the purpose of analyzing the impact of heterogeneity on reservoir performance, two test cases have been created. Again, the SPE10 benchmark test was used. The top 21 and bottom 21 layers have been taken from the model, and were resized to fit on the 51×51 grid. The top and bottom test cases will be referred to as SPE10-T and SPE10-B, respectively. Since the permeability range of this benchmark is very wide, it has been scaled down accordingly. To this end, the following relation is used:

$$\log k_{\text{scaled}} = \frac{\log k - \log k_{\text{min}}}{\log k_{\text{max}} - \log k_{\text{min}}} \cdot (\log k^*_{\text{max}} - \log k^*_{\text{min}}) + \log k^*_{\text{min}} \,. \tag{5.1}$$

Here, k_{min} and k_{max} are the minimum and maximum values of the original permeability field. k^*_{min} and k^*_{max} are the minimum and maximum values of the selected permeability range. In this case, their values are 10^{-15} and 10^{-13} m^2. The resulting permeability fields for the top 21 layers (SPE10-T) are depicted in Fig. 5.3. For the bottom 21 layers (SPE10-B), see Fig. 5.4.

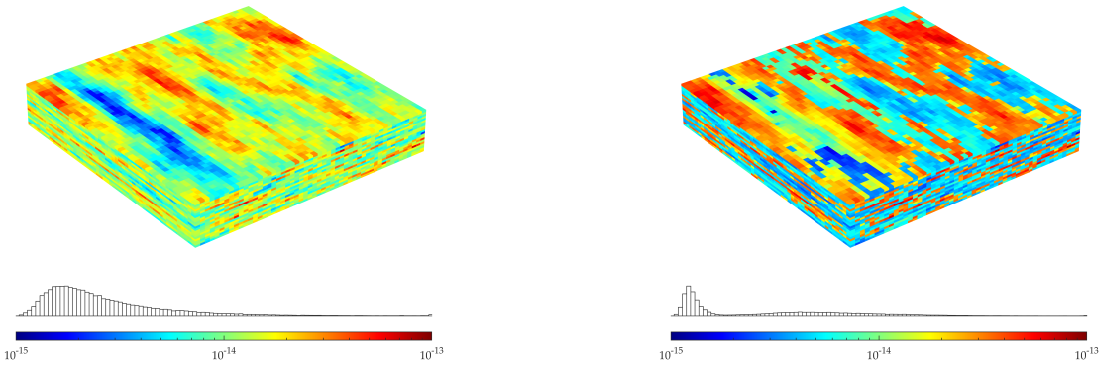

(a) (b)

Figure 5.3: Rescaled permeability (in m^2) and its distribution in (a) horizontal and (b) vertical direction for the top 21 layers of the SPE10 model.

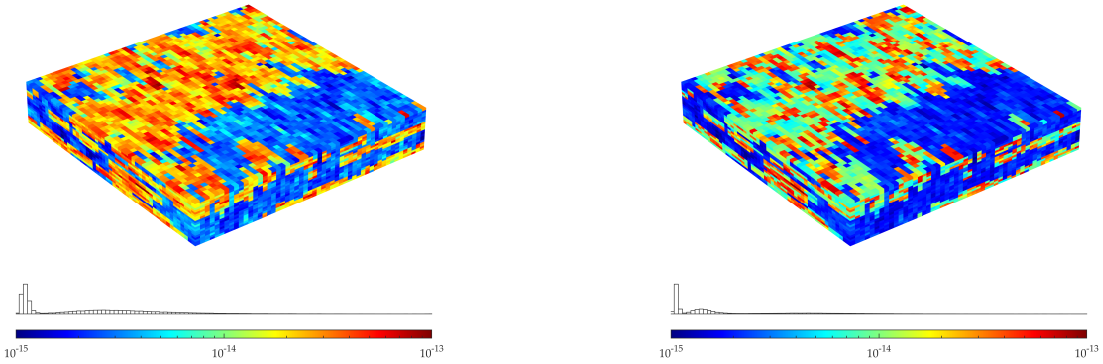

(a) (b)

Figure 5.4: Rescaled permeability (in m^2) and its distribution in (a) horizontal and (b) vertical direction for the bottom 21 layers of the SPE10 model.

5.2.5. Relative permeability

Relative permeability, introduced in Chapter 2, is fundamental in understanding flow behaviour in porous media. It describes the ability of each fluid phase to flow as a function of its saturation. The shapes of the relative permeability curves govern the efficiency of the displacement. As hydrogen is pumped into the reservoir, the governing equations follow the primary drainage curve (red in Fig. 5.5A), up until the point where S_g reaches its maximum value, $S_{g,max}$, represented by the dotted vertical line. In case of decreasing S_g after this point, the governing relations follow the primary imbibition curve (blue in Fig. 5.5A), until $k_{rg} = 0$ at $S_g = S_{gr}$. In the case that imbibition starts before S_g reaches $S_{g,max}$, the continuity of the transition is ensured by the use of scanning curves (see Fig. 5.5B) [40, 13, 58]. The scanning curves are based on the primary drainage and imbibition curves, which are referred to as bounding curves. The transitional point is is S_{gt}, and its corresponding residual saturation S_{gr} (i.e. where $k_r = 0$) is found using the following linear relation [71]:

$$S_{gr} = f_r \cdot S_{gt} \,. \tag{5.2}$$

Here, f_r is a constant such that $f_r \leq 1$. For the purpose of this analysis, the value of f will be varied, mimicking different relative permeability scenarios. In the base case, its value is 0.5. For the first comparison, its value is set to 0.2 and for the second it is equal to 0. This means that for drainage and imbibition, the same curves are

employed.

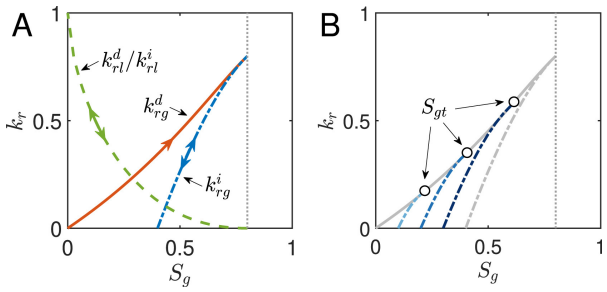

Figure 5.5: Illustration of hysteretic behaviour of relative permeability curves. (A) Primary drainage/imbibition curves for liquid and gas phases, where the superscripts d and i denote drainage and imbibition, respectively. A single/double-headed arrow indicates that the process along a given curve is irreversible/reversible, respectively. (B) Scanning curves generated at the turning point given by S_{gt} = 0.2, 0.4, and 0.6 [79].

5.2.6. Anticline

An anticline is defined as a structural feature in which rock has been bent into an arch-like shape. If the caprock is sufficiently low in permeability, such a formation can make for the trapping of hydrogen. In this example, the impact of the degree of anticline will be analyzed. Therefore, two variations on the base case have been made. One with a flatter angle of 9 degrees, and another reservoir with a steeper angle of 38 degrees. The anticline angles are calculated as:

$$\theta = \arctan\left(\frac{h}{l_x/2}\right), \tag{5.3}$$

where h is the height of the dome and l_x is the reservoir dimension in x direction. In Fig. 5.6, a cross-section of the three reservoirs is shown.

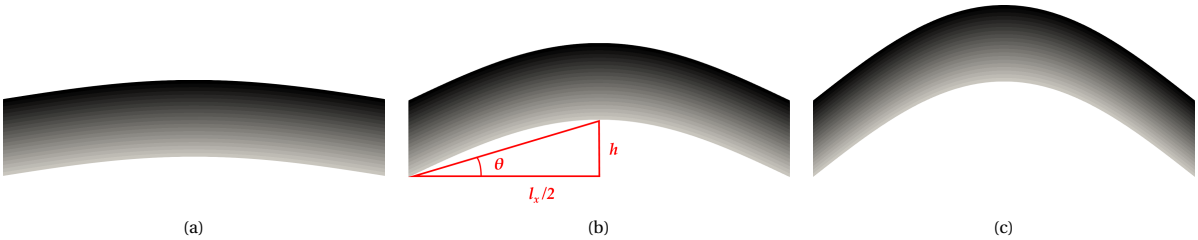

Figure 5.6: Cross section of reservoirs with anticline angle (a) 9°, (b) 25°, and (c) 38°.

5.2.7. Cushion gas

The primary purpose of cushion gas is to maintain pressure inside the reservoir for cyclic injection and production of the working gas. In depleted gas reservoirs, the hydrogen can be pressurized using the leftover native gases. For aquifers however, it is required to inject another gas for pressurization. Commonly considered gases are methane (CH_4), carbon dioxide (CO_2) or nitrogen (N_2) [37]. In this test, hydrogen is used as the cushion gas. The first injection period for the test is extended, effectively replicating a cushion gas injection. It will be extended by 1 month in this test. Figure 5.7 provides an overview of the adjusted cyclic scheme. For the calculation of the recoverability, the cushion gas injection period will be neglected.

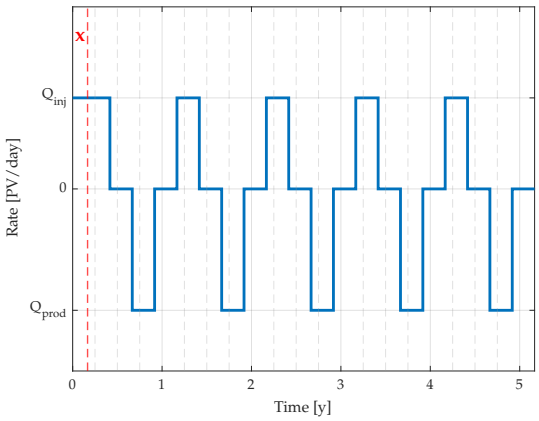

Figure 5.7: Adjusted cyclic scheme for operation with cushion gas. The duration of the cushion gas injection period is denoted by x.

5.2.8. Summary

In Table 5.2, all the variations on the base case are tabulated. The gray row represents the base case. Every other cell stands for a separate test case. In total, 13 different cases (not including the base case) are simulated.

Table 5.2: Overview of all alterations made to the base case. Note that every cell, except for the ones in the gray row, represents a separate test case.

PARAM. / TEST	ANISOTROPY	ANTICLINE	CUSHION GAS	HETEROGENEITY	PERM.	PORO	REL. PERM.
Base	$k_v/k_h = 0.1$	$\theta = 25°$	No c.g.	Homogeneous	$k = 100$ mD	$\phi = 0.2$	$f = 0.5$
1	$k_v/k_h = 0.5$	$\theta = 9°$	1 month	SPE10-T	$k = 10$ mD	$\phi = 0.1$	$f = 0.2$
2	$k_v/k_h = 1$	$\theta = 38°$	-	SPE10-B	$k = 1000$ mD	$\phi = 0.3$	$f = 0$

5.3. Results

In this section, the reservoir performance sensitivity analysis will be discussed. The reservoir performance will be based mainly on the recoverability. Recoverability is defined as the gravimetric ratio between the hydrogen that has been produced and the hydrogen that has been injected during operational cycle i:

$$R_i = \frac{M_{prod,i}}{M_{inj,i}} \cdot 100\,, \quad i \in (1,\ldots,n)\,; \tag{5.4}$$

with n being the total number of cycles.

5.3.1. Porosity

Here, the results for porosity analysis will be discussed. In Fig. 5.8, the mass fraction of each of the different states for the three test cases is shown. From this figure, it is clear that the amount of immobile gas is related to the porosity of the reservoir. With lower porosity, there is less pore volume (PV) for the hydrogen to get immobilized by, leading to a lower mass fraction in the immobile state. It is also worth noting the sharp increase in immobile mass fraction after the injection period ends, during cycles 4 and 5.

Additionally, since the same volume of hydrogen has been injected into three distinct PVs for each of the tests, the plume size varies significantly. An overview of plume size is shown in Fig. 5.9.

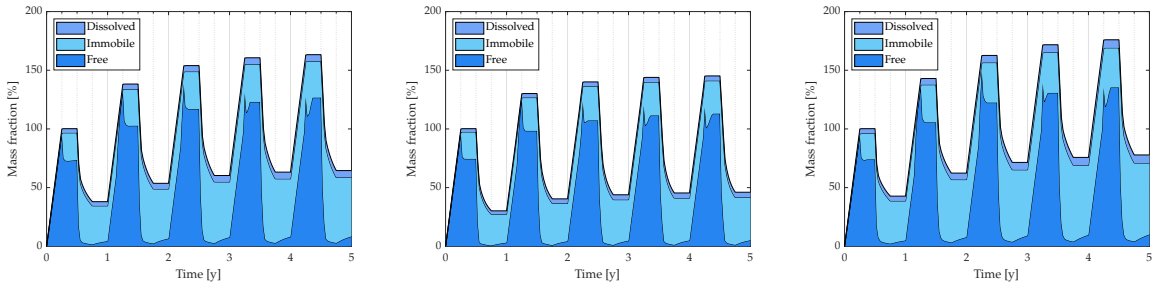

Figure 5.8: Normalized mass fractions for hydrogen in free, immobile, and dissolved states. (a) Base case with $\phi = 0.2$, (b) Test case 1 with $\phi = 0.1$, (c) Test case 2 with $\phi = 0.3$. The mass fractions are normalized against the total H_2 mass in the reservoir at the end of the first injection period, at $t = 90$ days.

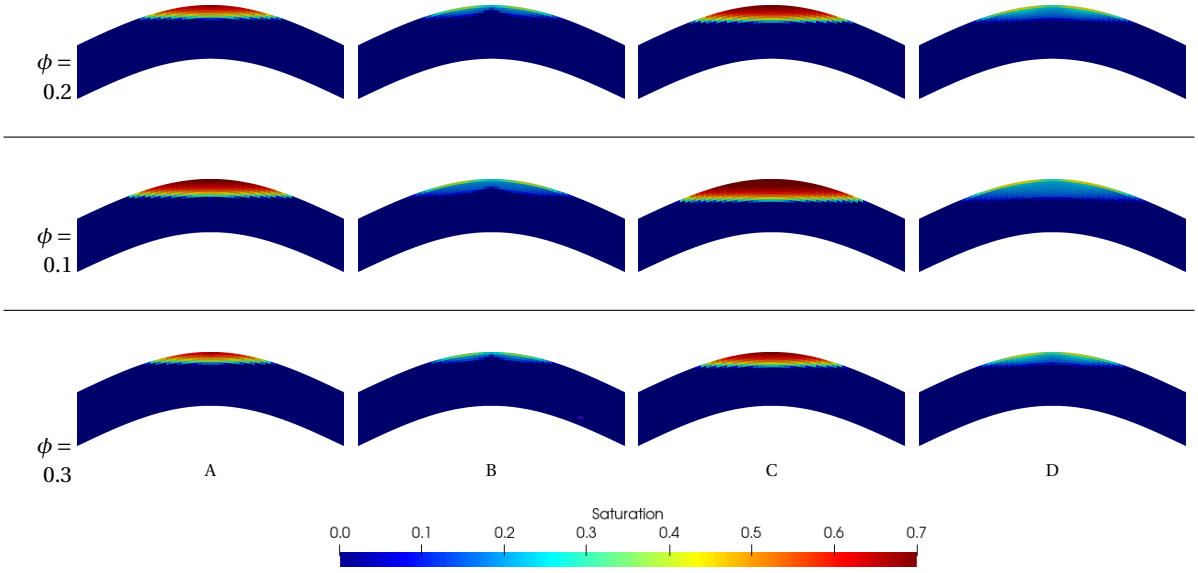

Figure 5.9: Hydrogen plume migration for the base case with $\phi = 0.2$, test case 1 with $\phi = 0.1$, and test case 2 with $\phi = 0.3$ at (A) end of first injection cycle, (B) end of first production cycle, (C) end of last injection cycle, and (D) end of last production cycle.

The resulting recoverabilities are shown in Fig. 5.10. For the simulation with lower porosity, the recoverability is consistently higher than the base case. The initial recoverability is 69.99%, which is 12.5% higher than the base case. For the last cycle, the difference is less distinct, with recoverability values of 99.6 and 98.9% for $\phi = 0.1$ and the base case, respectively. Notably, the recoverability for the reservoir with $\phi = 0.3$ is lower for all cycles, compared to the base case. Initially, it is 7.6% lower. During the fifth cycle, the recoverability is 0.8% below that of the base case.

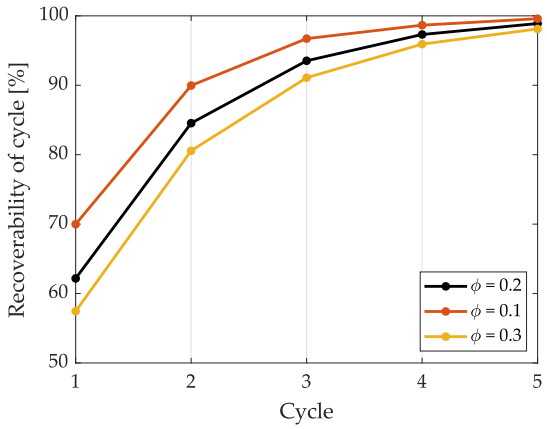

Figure 5.10: Recoverability rates for test cases with $\phi = 0.1,\ 0.2,$ and 0.3.

5.3.2. Permeability

This section will discuss the results for simulations with varying values for permeability. For the three cases, there is a clear difference visible in Fig. 5.11. It shows that in less permeable reservoirs, more hydrogen gets immobilized. For reservoirs with higher permeability, the opposite is the case. This is because of capillary forces, allowing the hydrogen to get bypassed and surrounded by water after injection ends. This leaves the hydrogen trapped and immobile. The resulting recoverabilities for each of the test cases are displayed in Fig. 5.12. The rates vary significantly, especially for the case with $k = 10$ mD. For the first cycle, the recoverability rate is 20.9% lower than that of the base case. As for the case with $k = 1000$ mD, recoverability is initially 20.8% higher than the base case. The difference reduces to 2% during the final cycle. The recoverability rate during the last cycle is equal to 100.9%, producing more than was injected. These results are in agreement with the literature, where commonly a minimum permeability of 50 mD is suggested for proper reservoir performance [64].

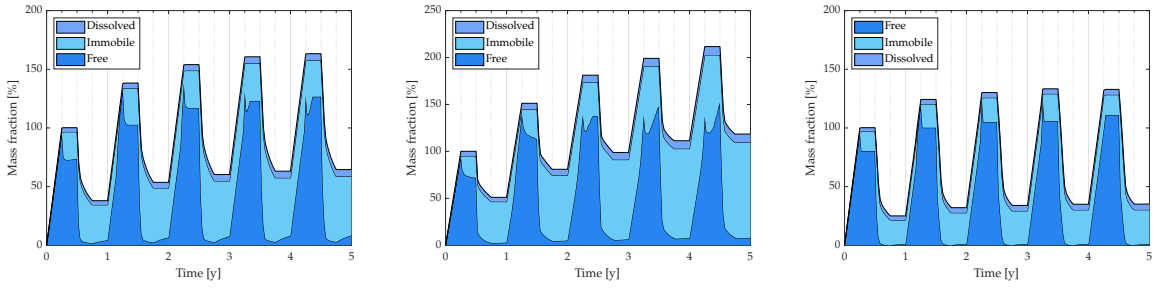

Figure 5.11: Normalized mass fractions for hydrogen in free, immobile, and dissolved states. (a) Base case with $k = 100$ mD, (b) Test case 1 with $k = 10$ mD, (c) Test case 2 with $k = 1000$ mD. The mass fractions are normalized against the total H_2 mass in the reservoir at the end of the first injection period, at $t = 90$ days.

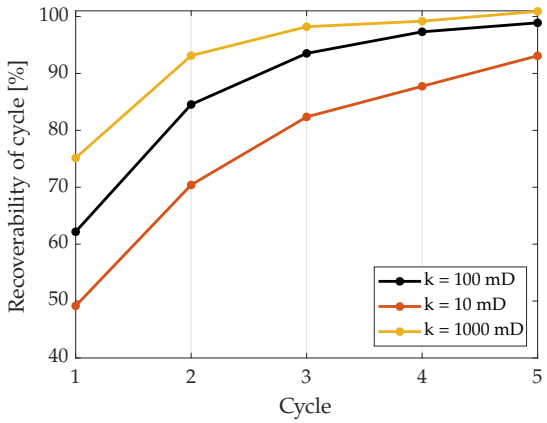

Figure 5.12: Recoverability rates for test cases with $k = 100,\ 10,$ and 1000 mD.

5.3.3. Anisotropy

Here, results for different anisotropy rates will be discussed. As stated in Section 5.2.3, the ratio between vertical and horizontal permeability defines the anisotropy rate. For the base case, a value of 0.1 is used, for test 1 it is equal to 0.5 and for test 2 the reservoir is fully isotropic, i.e. the anisotropy rate is equal to 1.0. For higher values of anisotropy rate, the hydrogen can flow more uniformly inside the reservoir. It is therefore expected that higher anistropy rates lead to higher recoverability rates. From Fig. 5.13, it can be observed that higher anisotropy rates result in lower immobile mass fraction. This is due to the fact in reservoir with low anisotropy rate (k_v/k_h) gas migrates laterally, since vertical permeability is relatively low. For the hydrogen, this effectively creates more opportunity to get trapped and immobilized. In contrast to the base case, in both test cases, the immobile fraction during cycles 4 and 5 does not show a sharp increase right after the injection period ends. In anisotropic reservoirs, vertical hydrogen distribution is less connected. This means that, when injection is terminated, water flows back and isolates the gas. This phenomenon is referred to as *snap-off* [41] and causes a sharp increase in immobile gas fraction when injection stops. More isotropic reservoirs are better connected in all directions, causing the water to imbibe more smoothly, resulting in a less sudden increase in immobile gas. In Fig. 5.14, recoverability rates are displayed. During the first cycle, the recoverability is 3.6% higher for the more isotropic and fully isotropic reservoirs. The rates are 0.9% higher for the final cycle. Between the two tests, the differences are minor.

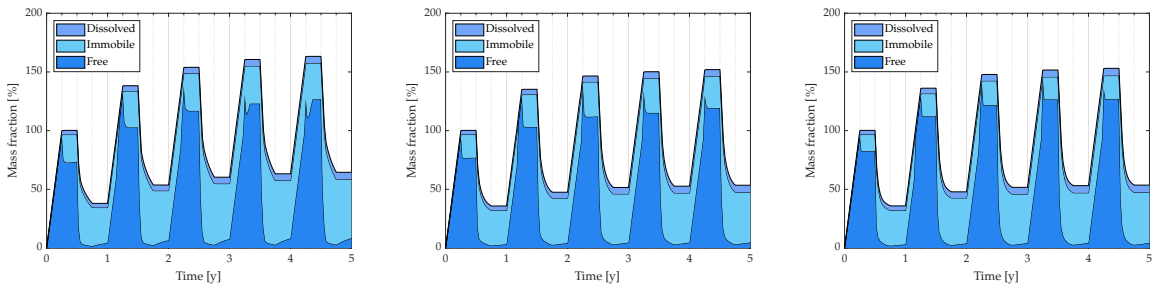

Figure 5.13: Normalized mass fractions for hydrogen in free, immobile, and dissolved states. (a) Base case with $k_v/k_h = 0.1$, (b) Test case 1 with $k_v/k_h = 0.5$, (c) Test case 2 with $k_v/k_h = 1.0$. The mass fractions are normalized against the total H_2 mass in the reservoir at the end of the first injection period, at $t = 90$ days.

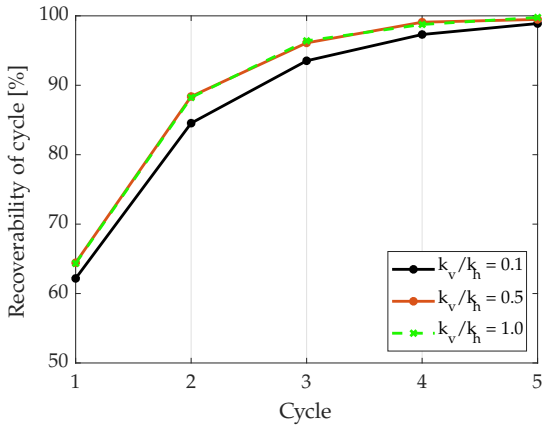

Figure 5.14: Recoverability rates for test cases with $k_v/k_h = 0.1,\ 0.5,$ and 1.0.

5.3.4. Heterogeneity

For the heterogeneous test cases, permeability fields from the SPE10 benchmark test were employed. In Fig. 5.15, the normalized mass fractions for each of the three cases are shown. From the figures, it is clear that heterogeneity negatively affects the fraction of free hydrogen in the reservoir, harming recoverability rates. Since the hydrogen plume migration is not uniform for the heterogeneous cases (see Fig. 5.16), the mass fraction of hydrogen made immobile is also higher. The recoverability rates for each of the cases are shown in Fig. 5.17. The difference in recoverability is most prominent during the first cycle, where the recoverabilities for the SPE10-T and SPE10-B cases are 12.8 and 14.8% lower compared to the base case, respectively. During the last cycle however, recoverabilities are similar, ranging from 97.99% for the SPE10-T case to 98.89% for the base case. It should be noted that, although these two test cases report lower recoverability for all cycles, there may exist heterogeneous permeability fields in which hydrogen displays better recoverability. For example, well-connected zones with high permeability could lead to more efficient withdrawal of hydrogen during production phases, enhancing reservoir performance.

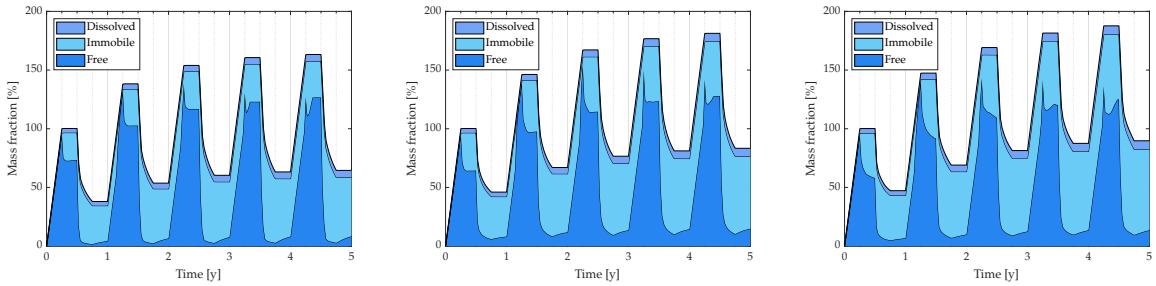

Figure 5.15: Normalized mass fractions for hydrogen in free, immobile, and dissolved states. (a) Homogeneous base case, (b) SPE10-T case, (c) SPE10-B case. The mass fractions are normalized against the total H_2 mass in the reservoir at the end of the first injection period, at $t = 90$ days.

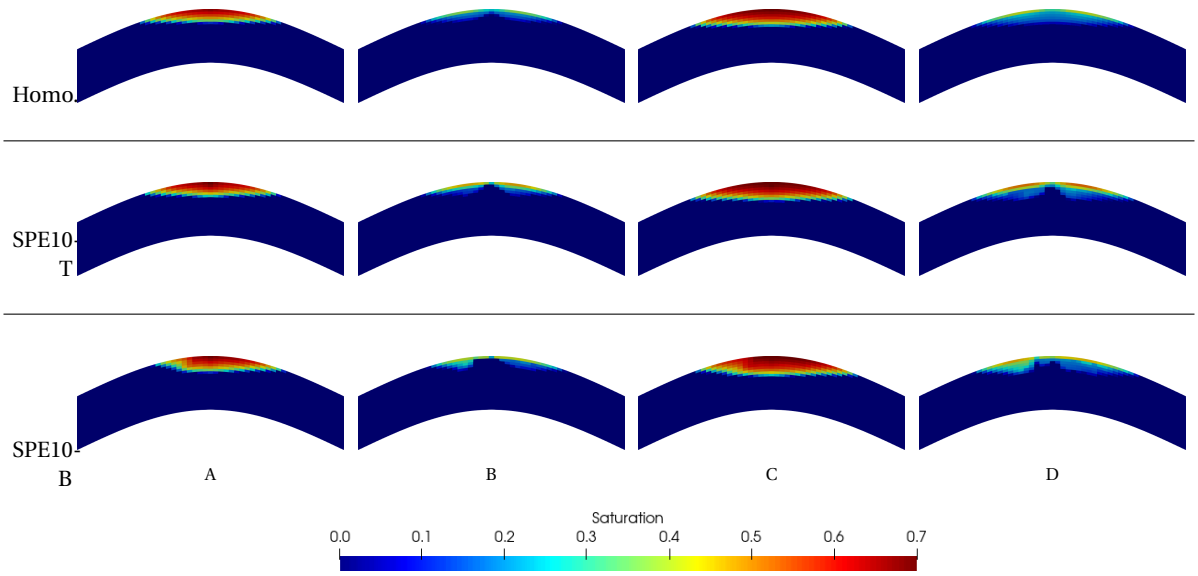

Figure 5.16: Hydrogen plume migration for the homogeneous case, SPE10-T case, and SPE10-B case at (A) end of first injection cycle, (B) end of first production cycle, (C) end of last injection cycle, and (D) end of last production cycle.

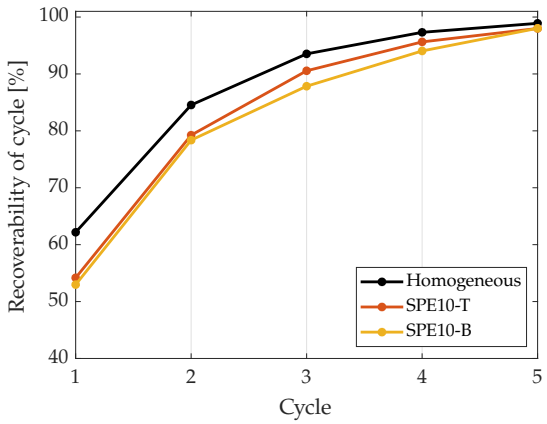

Figure 5.17: Recoverability rates for homogeneous, SPE10-T, and SPE10-B case

5.3.5. Relative permeability

In this section, the results for relative permeability will be discussed. As described in Section 5.2.5, the relative permeability was varied based on the constant f_r, which linearly relates the residual saturation S_{gr} and the saturation at the turning point from primary drainage to primary imbibition S_{gt}. In the base case, its value is equal to 0.5, and in test 1 and 2, it was set to 0.2 and 0, respectively. Since in test case 2, the primary drainage and primary imbibition curves are the same, it is expected that no hydrogen is left immobile during the simulations. The mass fractions for free, immobile, and dissolved hydrogen for each of the test cases are shown in Fig. 5.18. For $f_r = 0$, the immobile mass fraction during the simulation is indeed equal to 0. It can be observed that (part of) the immobile mass fractions are replaced by free hydrogen for each of the test cases. The recoverability rates are shown in Fig. 5.19. For both of the test cases, the recoverability rates are lower for every cycle. The recoverability rates for both test cases are almost identical, differing by 0.3% and 0.1% at the first and last cycle, respectively. The base case rate is 6.6% higher during the first cycle, and 0.7% higher during the last cycle.

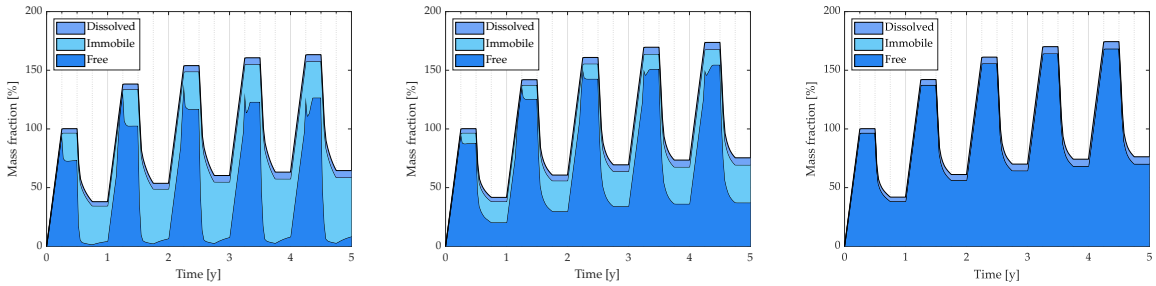

Figure 5.18: Normalized mass fractions for hydrogen in free, immobile, and dissolved states. (a) Base case with $f_r = 0.5$, (b) Test case 1 with $f_r = 0.2$, (c) Test case 2 with $f_r = 0$. The mass fractions are normalized against the total H_2 mass in the reservoir at the end of the first injection period, at $t = 90$ days.

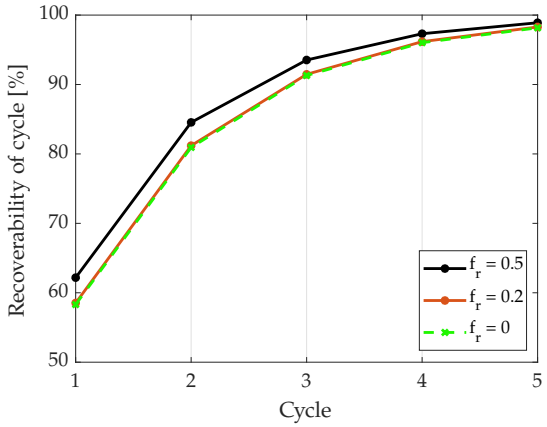

Figure 5.19: Recoverability rates for test cases with $f_r = 0.5$, $f_r = 0.2$, and $f_r = 0$.

5.3.6. Anticline

For different degrees of anticline, it is expected that the reservoir with the steepest anticline performs the best. This is because the hydrogen gets trapped by the anticline and is thus better recoverable. Here, the most obvious difference is in the dissolved portion of the hydrogen. When hydrogen dissolves into the brine, it can no longer be recovered. From Fig. 5.20, it is clear that with a shallower anticline, more hydrogen gets dissolved into the brine. Since the hydrogen plume migrates further horizontally for the reservoir with shallower anticline, as can be observed in Fig. 5.21, the hydrogen has more contact area with the brine, leading to higher dissolved mass fraction. Similarly, a shallower anticline yields more immobile gas. Especially during the first 2 cycles, the mass fraction increases significantly for the reservoir with $\theta = 9°$. The recoverability rates are shown in Fig. 5.22. For the reservoir with a shallower angle, the hydrogen was 19% less recoverable during the first cycle, and 1.8% less recoverable during the last cycle. In the steeper angled reservoir, rates were 5.8 and 0.5% higher during the first and last cycle, respectively.

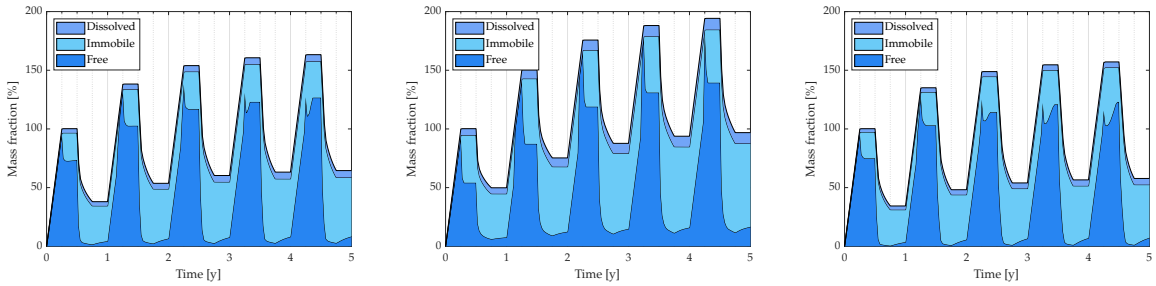

Figure 5.20: Normalized mass fractions for hydrogen in free, immobile, and dissolved states. (a) Base case with $\theta = 25°$, (b) Test case 1 with $\theta = 9°$, (c) Test case 2 with $\theta = 38°$. The mass fractions are normalized against the total H_2 mass in the reservoir at the end of the first injection period, at $t = 90$ days.

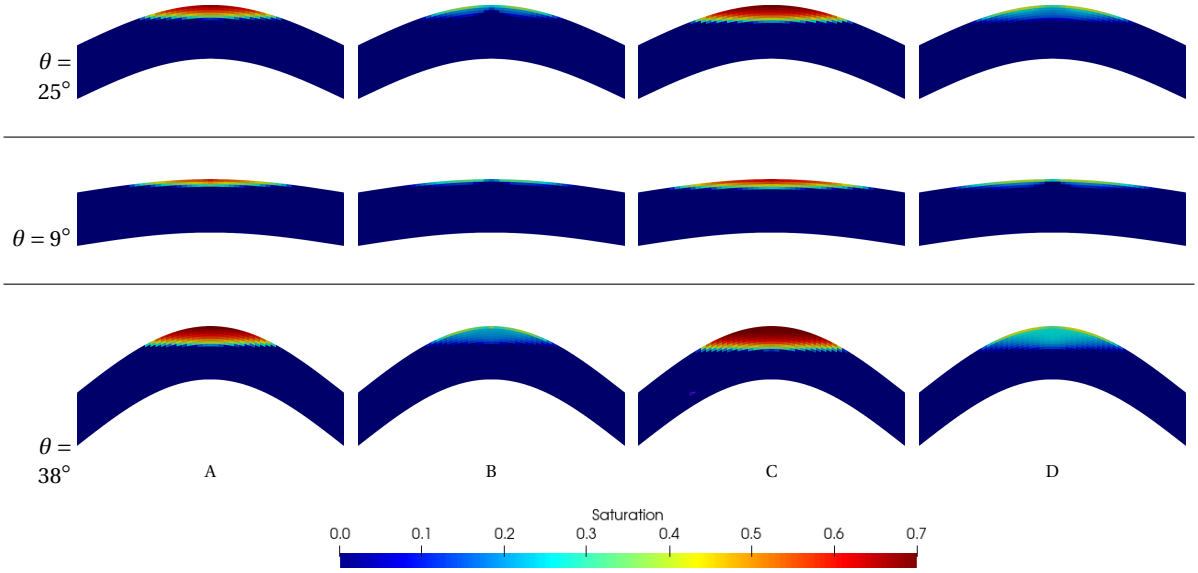

Figure 5.21: Hydrogen plume migration for the base case with $\theta = 25°$, test case 1 with $\theta = 9°$, and test case 2 with $\theta = 38°$ at (A) end of first injection cycle, (B) end of first production cycle, (C) end of last injection cycle, and (D) end of last production cycle.

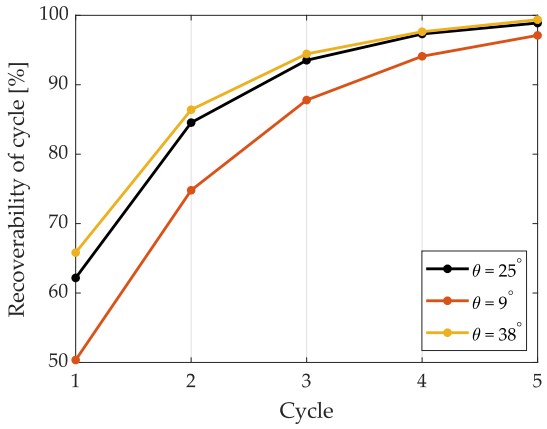

Figure 5.22: Recoverability rates for test cases with $\theta = 25°$, $\theta = 9°$, and $\theta = 38°$.

5.3.7. Cushion gas

As described in Section 5.2.7, the main purpose of the cushion gas is to pressurize the reservoir. In effect, this increase in pressure inside the reservoir is expected to enhance recoverability. In this single test case, the first injection period was elongated by one month. This pre-injected hydrogen serves as the cushion gas. The mass fractions are given in Fig. 5.23. Note that the red line in Fig. 5.23b represents the normalized hydrogen volume after cushion gas injection. The corresponding recoverability rates are calculated from this line. They are shown in Fig. 5.24. Especially during the first two cycles, the jump in recoverability rate is obvious. Initially, the recoverability rate is 31.4% higher. During the second cycle, it is 9.8% higher. During the last cycle, their values are nearly identical, differing by 0.2%.

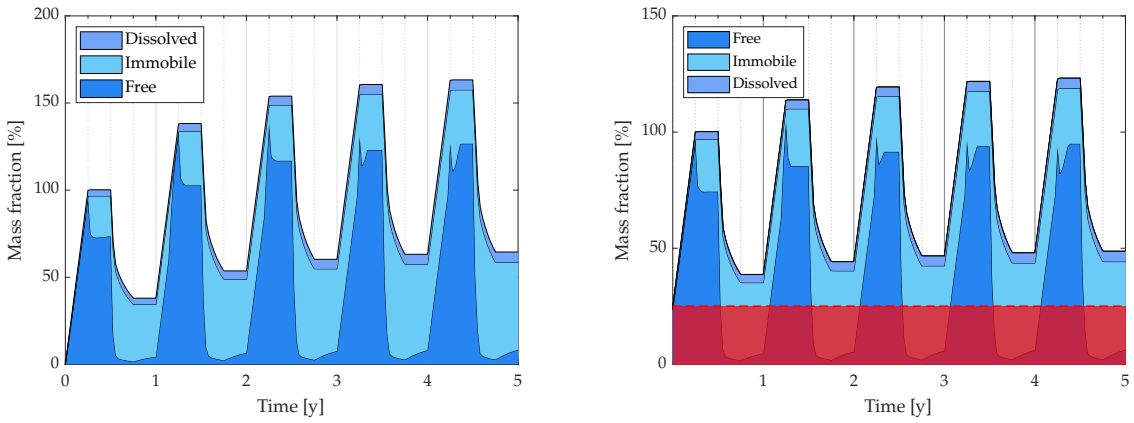

Figure 5.23: Normalized mass fractions for hydrogen in free, immobile, and dissolved states. (a) Base case without cushion gas, (b) Test case 1 with cushion gas injected. For (b), the recoverability rate is calculated from the red line. The mass fractions are normalized against the total H_2 mass in the reservoir at the end of the first injection period, at t = 90 days (a) and t = 120 days (b).

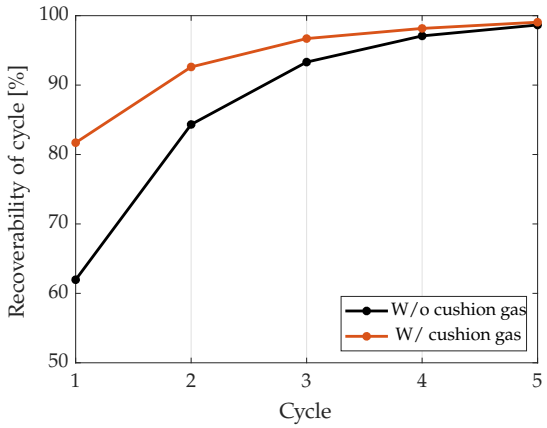

Figure 5.24: Recoverability rates for simulation with and without cushion gas.

5.3.8. Summary

For all of the test cases, it can be observed that recoverability rate increases as the injection and production cycles progress. In its initial state, the reservoir is fully saturated with brine. As hydrogen is injected, a substantial amount of hydrogen is lost due to dissolution and residual trapping. For the following cycles, a portion of the reservoir pores has already trapped hydrogen. Similarly, part of the brine has already been saturated

with dissolved hydrogen. This reduces the opportunity for hydrogen to get trapped and dissolved. Therefore, more hydrogen remains recoverable. Additionally, in the test cases, water upconing was observed [55]. Water upconing is defined as the cone-like shape that the hydrogen-brine interface forms when hydrogen withdrawal rates are substantially high. This high rate of hydrogen withdrawal is necessary due to the low volumetric energy density of hydrogen. In effect, it may cause brine to mix with the hydrogen during production, decreasing the purity of the produced hydrogen. An example of water upconing in the base test case is given in Fig. 5.25.

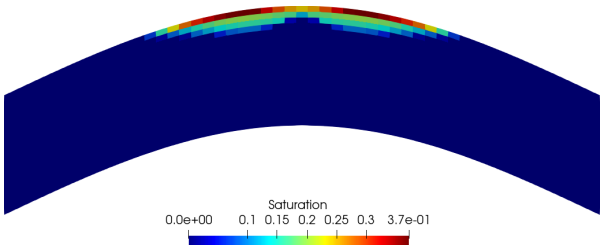

Figure 5.25: Example of water upconing in base case test reservoir after first production period.

For every cycle, the relative change in recoverability rate for all 13 test cases is depicted in Fig. 5.26. From the figure, it is clear that the impact of the varied parameters decreases as more injection and production cycles are completed. This can again be explained by the fact that during the first cycles, a larger share of hydrogen gets residually trapped or dissolved in the brine. Changes to reservoir parameters, therefore, have a more pronounced impact on recoverability during the initial cycles. However, the effects of reduced permeability and a shallower anticline continue to influence the recoverability for the entire duration of the simulation. This underlines the significance of permeability and reservoir geometry in determining long-term reservoir performance.

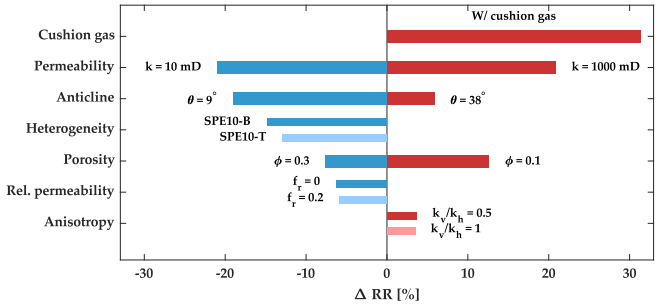

(a)

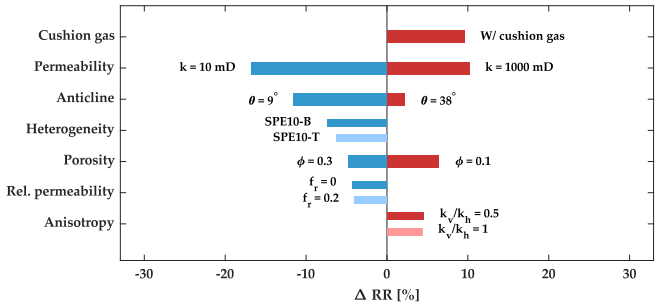

(b)

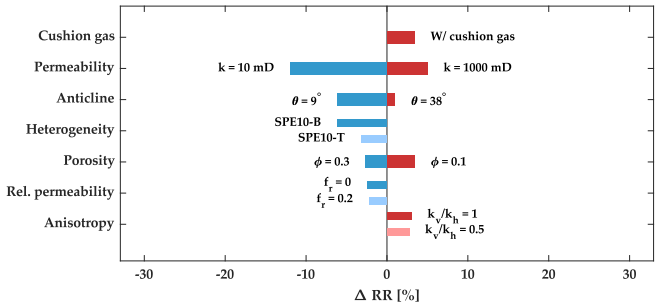

(c)

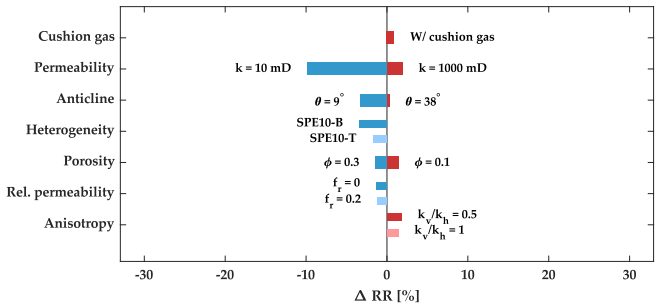

(d)

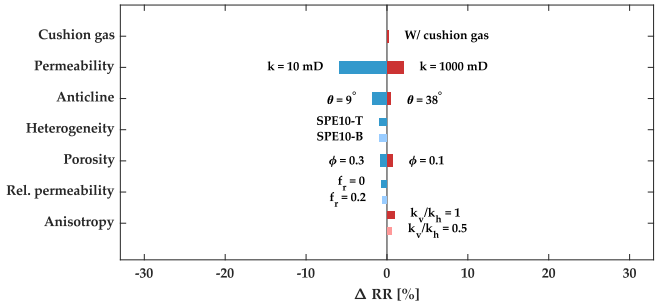

(e)

Figure 5.26: Relative change in recoverability rate (RR) for all 13 test cases with respect to the base case for (a) first, (b) second, (c) third, (d) fourth, and (e) fifth cycle.

6

SUBSURFACE HYDROGEN STORAGE ON FIELDSCALE

As described in Chapter 1, large-scale energy storage systems are deemed necessary to address the intermittency of renewable energy sources. In this chapter, the possibilities and performance of a large-scale energy storage system in the form of a subsurface hydrogen storage site are explored. For this purpose, the Johansen formation near the coast of Norway will be utilized.

6.1. Johansen formation

The Johansen formation is a large saline aquifer in the Northern North Sea, off the South Western coast of Norway. It has been part of both MatMoRA (Mathematical Modelling and Risk Analysis) [67] research projects on geological CO_2 storage. The aim of this project was to develop analytical and numerical tools with which risk assessment analysis of geological storage of CO_2 could be performed. Funding of the project was provided by the Climit programme [25] at the Research Council of Norway and by industry partners. Academic partners were the University of Bergen (UiB), Uni Research AS (CIPR), and SINTEF ICT. Of the Johansen formation, 3D seismic data has been collected by the Norwegian Petroleum Directorate (NPD), based on which a CPG model of the field has been realized. The formation is part of the Lower Jurassic Dunlin group. On both top and bottom, the formation is covered by shale layers with very low permeability, acting as a caprock. The formation itself consists of sandstone and has moderate permeability, ranging from 60 to 1 660 mD, and an average porosity of around 25%. The formation lies at depths from 2 200 to 3 400 meters below sealevel and has an average thickness of about 100 meters. It spans nearly 60 kilometers latitudinally and 100 kilometers longitudinally. These characteristics make for a promising theoretical CO_2 storage capacity of over 1 Gt [21].

6.1.1. Dataset

As described above, 3D seismic data has led to the creation of a number of geological models of the Johansen formation. In total, five models have been created: a full-field model, three homogeneous sector models, and a heterogeneous sector model (NPD5). The latter will be used for this analysis. The model consists of 1 100 000 cells, with $n_x = n_y = 100$ and $n_z = 11$. Of these cells, 887 775 are marked as active. The reason for this difference is the fact that the CPG grid needs to be projected on a regular Cartesian basis. So, when the grid has an irregular shape, cells are added and later set as inactive to conform to this requirement. This way, they are not included in the simulation itself. In Fig. 6.2, the active part and the faults of the NPD5 model are shown.

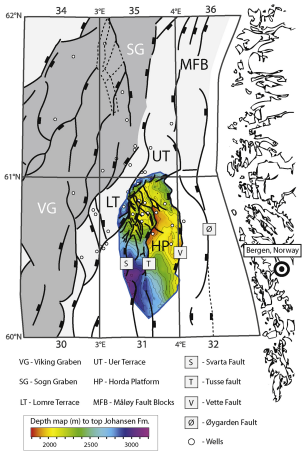

Figure 6.1: Structural map of the Johansen field and its surrounding area [73].

(a) (b)

Figure 6.2: Illustration of the (a) active part (yellow) and (b) faults (red) of the NPD5 sector of the Johansen formation.

6.1.2. Petrophysical data

In the NPD5 dataset, the Johansen formation is represented by 11 layers in the vertical direction. The formation is covered by the Amundsen [60] shale below, and by the Dunlin [14] shale above. In the model, the Amundsen and Dunlin shale are represented by six and one layer(s) in z-direction, respectively. In Figs. 6.3 and 6.4, the porosity and permeability for both the whole NPD5 model and the sandstone within it are shown. The permeability is assumed to be isotropic in this case.

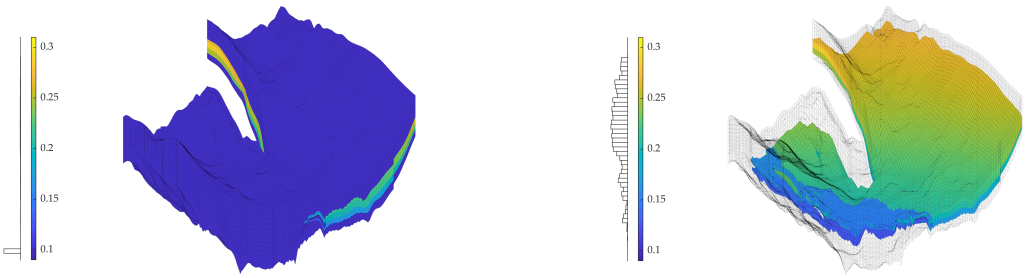

(a) (b)

Figure 6.3: Visual representation of porosity and its distribution of the NPD5 model, for (a) the whole model and (b) the model without shale layers. The dimensions in z-direction have been exaggerated by a factor 10.

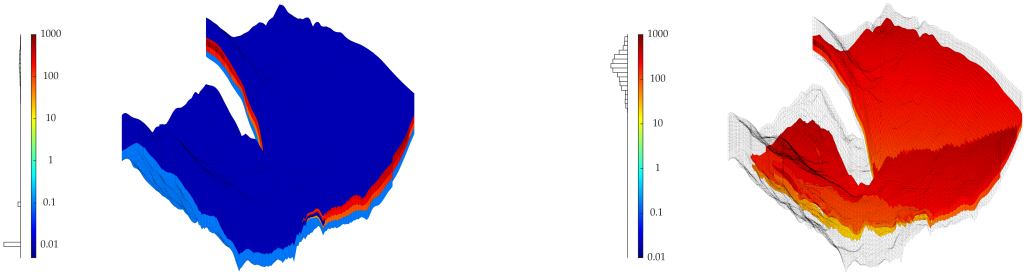

(a) (b)

Figure 6.4: Visual representation of permeability and its distribution of the NPD5 model, for (a) the whole model and (b) the model without shale layers, in mD. The dimensions in z-direction have been exaggerated by a factor 10.

6.2. Reservoir analysis

With the key geological and petrophysical characteristics of the reservoir now established, the reservoir performance and suitability for H_2 storage can be analyzed.

6.2.1. Well placement

An essential part of this analysis is the determination of suitable well placements. Well placement and spacing influence injectivity, recoverability and pressure management in the reservoir. Properly locating injection and production wells will ensure uniform distribution of hydrogen and minimize flow paths. Additionally, strategic well placement should account for reservoir heterogeneity as well as structural boundaries, while ensuring containment of the gas. Therefore, 10 potential injection well sites have been selected. For these sites, a simulation has been run under monotonous injection for a period of 150 days. For this simulation, cells with $k < 0.1$mD were excluded. These shale layers are assumed to represent caprock, which is not of interest for these simulations. This enables analysis of the spatial distribution of hydrogen within the reservoir. The analysis then supports the identification of suitable injection sites. Figure 6.5 provides an overview of the selected well sites. Table 6.1 lists their *(i, j)* indices and descriptions.

(a) (b)

Figure 6.5: Overview of tested injection well sites, in (a) 2D and (b) 3D.

Table 6.1: List of *(i,j)* indices and descriptions of well sites.

WELL SITE NO.	*(i, j)* INDEX	DESCRIPTION
1	(26, 12)	North-Eastern anticline
2	(66, 13)	North-West
3	(34, 10)	North near fault
4	(41, 45)	Middle near fault
5	(14, 48)	East-middle
6	(62, 51)	West-middle, low k
7	(73, 14)	North-West, low k
8	(18, 90)	South-East, low k
9	(26, 92)	South-East, high k
10	(46, 80)	South-West, low k

6.2.2. Results

After the simulation, the spatial distribution of the hydrogen within the reservoir is visually analyzed. For each of the injection well sites, the resulting saturation at $t = 150$ days is shown in Fig. 6.6.

From these results, it can be observed that the high buoyancy of hydrogen plays a critical role. For each of the sites, the hydrogen reaches a certain high, where the gas accumulates. This is critical for proper hydrogen storage, as the hydrogen gets trapped there by the shale layers covering the sandstone. Now, the potential injection sites can be narrowed down. Three promising storage sites are identified by these tests. They are listed in Table 6.2.

Table 6.2: Identified potential storage sites in Johansen reservoir.

STORAGE SITE	DESCRIPTION	IDENTIFIED BY WELL NO.:
A	North-Eastern high	1, 4, 5, 6, 8, 9, 10
B	North-Western anticline	2, 7
C	Northern high	3, 4

A visual representation of the well locations for the three storage sites is provided in Fig. 6.7.

Again, a simulation for 150 days is run for these three well locations. This way, it can be ensured that no hydrogen dissipates to other areas. In Fig. 6.8, it can be seen that the hydrogen is well confined within the three potential storage sites. Only for well location B, the hydrogen dissipates slightly into the surrounding formation. This can be explained by the fact that for these exploratory simulations, a high injection rate of $2.3462 \cdot 10^{-6}$ PV$\cdot$day^{-1} was used. Combined with the pore volume of the reservoir of $3.7571 \cdot 10^{10}$ m^3, this translates to a volumetric injection rate of nearly 90 000 m$^3 \cdot$day^{-1}.

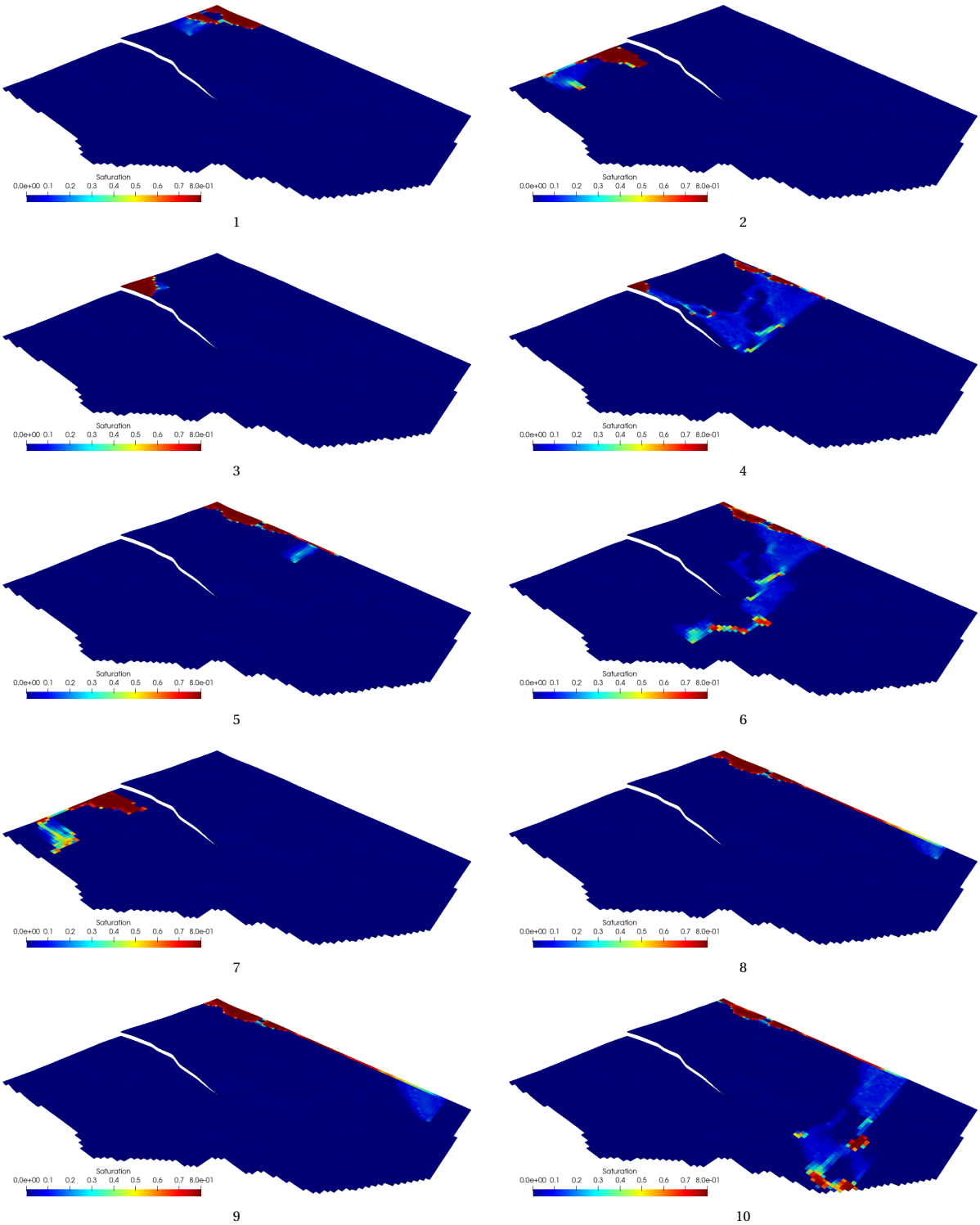

Figure 6.6: Hydrogen saturation profiles for each of the injection well configurations at $t = 150$ days.

(a) (b)

Figure 6.7: Overview of potential storage site well locations in (a) 2D and (b) 3D.

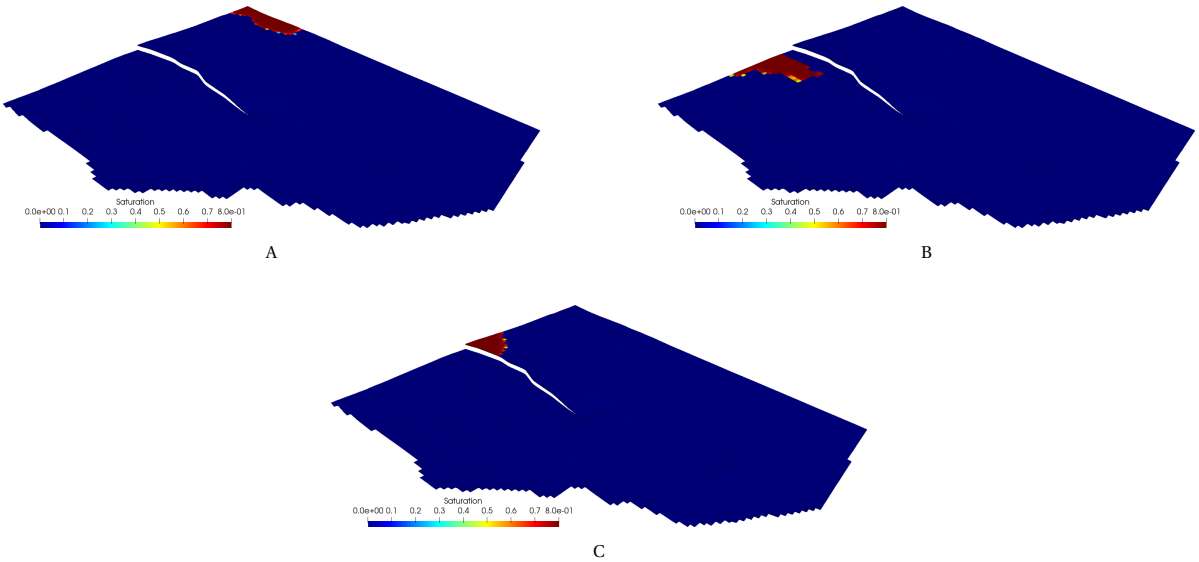

A B C

Figure 6.8: Hydrogen saturation at t = 150 days for well locations A, B and C.

6.3. Cyclic operation

In this section, the process of cyclic operation for each of the three storage sites shown in Fig. 6.7 will be described. The same cyclic scheme shown in Fig. 5.2a will be employed, where each period of injection and production is followed by an equally long idle time. Through an iterative process, the well locations for each storage site were refined. Also, injection and production rates for each site were adjusted separately. An overview of injection and production rates is given in Table 6.3.

Table 6.3: Overview of injection and production rates for each storage site, in PV·day^{-1}.

STORAGE SITE	Q_{inj}	Q_{prod}	PROD:INJ
A	$1.31 \cdot 10^{-8}$	$2.46 \cdot 10^{-5}$	1 880 : 1
B	$2.96 \cdot 10^{-8}$	$4.93 \cdot 10^{-5}$	1 667 : 1
C	$1.97 \cdot 10^{-8}$	$4.93 \cdot 10^{-5}$	2 500 : 1

For storage site A, the injection rate corresponds to an estimated stored amount of energy of 15 GWh per injection period. For sites B and C, it is equal to 33 and 23 GWh per injection period, respectively. These numbers are based on a gravimetric energy density of 33.3 kWh·kg^{-1} and a density of 10 kg·m^{-3} at reservoir conditions [54].

6.3.1. Results

For each potential storage site, in this section, the results will be discussed. Again, the performance of the storage site will be quantified in terms of recoverability rate, see Eq. (5.4).

Storage site A

For storage site A, 492 m^3 of hydrogen was injected per day of injection. The permeability in the region of the injection well ranges from 370 to 390 mD. Porosity is between 26 and 27%. The site was inclined at a shallow angle, with $\theta = 1°$. The mass fractions for hydrogen in each state are displayed in Fig. 6.9. From the figure, it is observable that a large portion of the hydrogen gets immobilized by snap-off. Still, the hydrogen proved recoverable, as can be concluded from Fig. 6.10. During the first cycle, the recoverability rate was equal to 58.9%. During the final two cycles, the recoverability rate was at 102.9 and 108.2%. The fact that more hydrogen was produced than was injected may be due to the high production rate. As was pointed out in Section 5.3.4, the heterogeneous distribution of permeability and porosity may have created preferential flow paths for hydrogen.

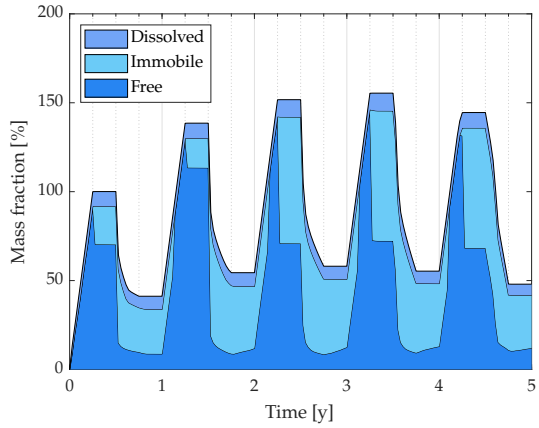

Figure 6.9: Normalized mass fractions of hydrogen in free, immobile, and dissolved state for storage site A. The mass fractions are normalized against the total H_2 mass in the reservoir at the end of the first injection period, at $t = 90$ days.

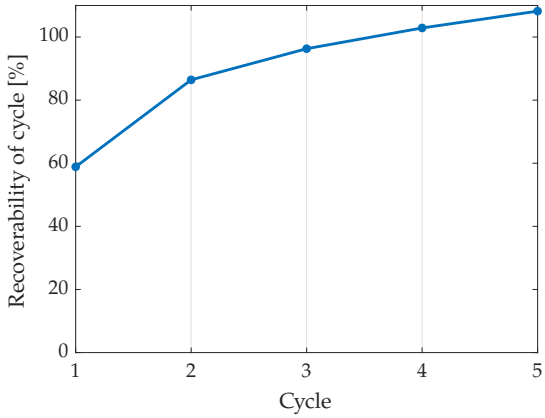

Figure 6.10: Recoverability rates for storage site A.

Storage site B

The anticline in storage site B is at its steepest point angled at $\theta = 9°$. Permeability ranges from 450 to 480 mD. The porosity ranges from 23 to 24%. For this storage site, an increased injection rate of 1 110 $m^3 \cdot day^{-1}$ has been applied. In Fig. 6.11, the mass fractions for free, immobile, and dissolved hydrogen in the reservoir are depicted. Here, it is noteworthy that a relatively large portion of hydrogen remains in the dissolved state. During the first cycle, this hinders recoverability, leaving 25.9% of hydrogen recoverable, shown in Fig. 6.12. In the subsequent cycles, the recoverability rates are significantly higher, consistently exceeding 95%. This consistency in recoverability may be explained by the high permeability inside the storage site, as well as the hydrogen being confined by the anticline.

Storage site C

In storage site C, permeability ranges from 300 to 380 mD. Porosity values range from 27 to 29%. Whereas the anticline angle measures only 0.7 degrees, the storage site is restricted by faults in the reservoir. An injection rate of 740 $m^3 \cdot day^{-1}$ is applied. The mass fractions of free, immobile, and dissolved hydrogen are shown in Fig. 6.13. It can be observed that the recoverability rates have dropped during the last two cycles. These are displayed in Fig. 6.14. During the first cycle, 61.8% of injected hydrogen is recoverable. This number increases to 99.2% for the third cycle. The hydrogen plume then reaches an area with higher permeability, where it can

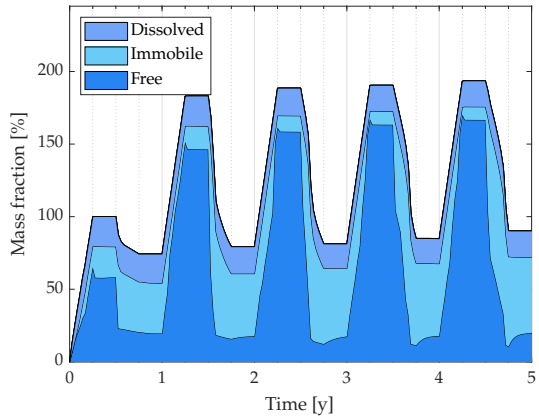

Figure 6.11: Normalized mass fractions of hydrogen in free, immobile, and dissolved state for storage site B. The mass fractions are normalized against the total H_2 mass in the reservoir at the end of the first injection period, at $t = 90$ days.

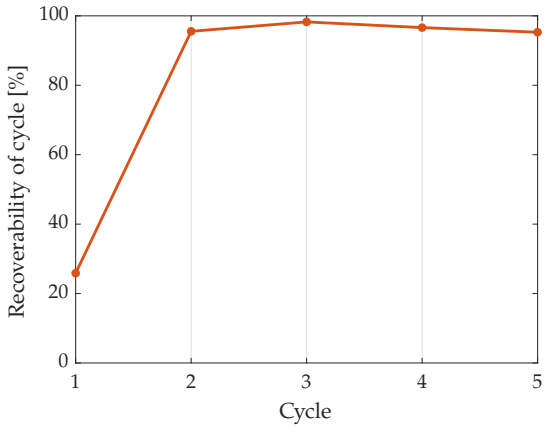

Figure 6.12: Recoverability rates for storage site B.

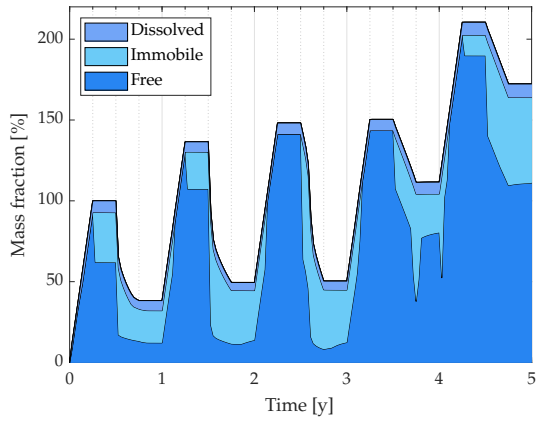

Figure 6.13: Normalized mass fractions of hydrogen in free, immobile, and dissolved state for storage site C. The mass fractions are normalized against the total H_2 mass in the reservoir at the end of the first injection period, at $t = 90$ days.

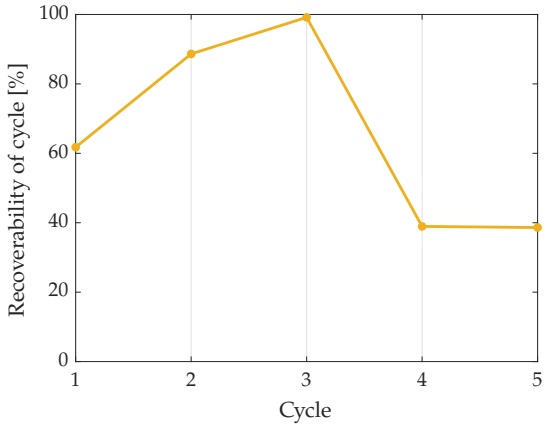

Figure 6.14: Recoverability rates for storage site C.

dissipate more easily. This causes the hydrogen to migrate away from the production well, resulting in a drop in recoverability, leaving 38.9 and 38.6% of hydrogen recoverable for the final two cycles.

6.3.2. Summary

For each of the three storage site locations, a different cyclic behaviour was observed. For example, in storage site B, recoverability rates stabilized after the first cycle to numbers above 95%. For storage site A, the recoverability rate steadily rose, producing more than was injected. On the other hand, in storage site C, rates dropped after the hydrogen plume had migrated away from the production well. All recoverability rates are shown in Fig. 6.15. The difference in recoverability and plume migration for each of the storage sites highlights the significance of site selection within a reservoir.

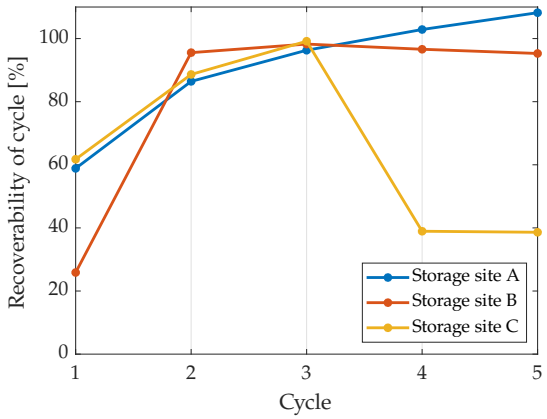

Figure 6.15: Recoverability rates for storage sites A, B, and C.

7

CONCLUSIONS AND FUTURE WORK

This final chapter presents the main conclusions that can be drawn from this thesis and outlines suggestions for future work. This thesis has aimed to identify reservoir parameters dictating reservoir performance and to demonstrate the identification of and operation of potential storage sites within a field-scale reservoir, as described in Chapter 1.

7.1. Conclusions

In the sensitivity analysis, seven parameters were varied, namely: porosity, permeability, anisotropy, anticline, heterogeneity, relative permeability, and the addition of cushion gas. Between these, the biggest improvement in recoverability rate was observed in the test case that featured cushion gas. This test demonstrated that cushion gas was able to adequately keep the reservoir pressurized, yielding a 30% increase over the base case in recoverability rate during the first cycle. Permeability of the reservoir also proved to be of substantial influence on reservoir performance. During the first cycle, both tests with more and less permeable reservoirs showed a deviation of 20% with respect to the base case. In contrast to the other tests, the recoverability rate in the less permeable reservoir remained substantially lower than the base case, reporting a difference of 6% in the last cycle.

Additionally, for the reservoir anticline, a steeper structure appears to be more favorable for hydrogen recovery during the initial cycles. In the test case with $\theta = 9°$, recoverability was 20% lower, whereas the steeper-angled reservoir showed a 5.8% increase in recoverability in the initial cycles.

From all test cases, it can be concluded that initially, reservoir parameters strongly influence the degree of recoverability. Reservoir permeability and anticline proved to have a lasting impact on hydrogen recoverability during subsequent cycles. When selecting sites for hydrogen storage, these parameters need careful consideration. Since the hydrogen not recovered during the initial cycle is effectively lost, ensuring a high recoverability rate from the outset is crucial for minimizing investment costs.

In the Johansen formation, the feasibility of subsurface hydrogen storage has been demonstrated. To this end, hydrogen dispersion has been analyzed for 10 distinct injection well locations distributed over the formation. Three potential hydrogen storage sites were identified from these exploratory simulations. It was ensured that hydrogen did not migrate away from these storage sites. Then, the seasonal hydrogen storage potential of the Johansen formation was demonstrated using a cyclic injection and production scheme. Quantities of stored energy ranged from 15 to 33 GWh per injection cycle. For two of the storage sites, recoverability rates of 95% and over were reported after the initial cycle. In the third example, the hydrogen migrated towards more

permeable parts of the storage site, from where it could be recovered to a lesser extent, emphasizing the need for precise well placement and geological site selection.

7.2. Future work

In this section, several suggestions for future work are made. In analyzing the reservoir performance sensitivity, only two tests were performed per parameter. The analysis could have been made more extensive by including more variants per parameter. Secondly, a fixed injection and production scheme has been used for all simulations, which limits the overall scope of this work. It may be that, for certain reservoir configurations, an alternative cyclic scheme yields better reservoir performance. Shorter idle times, for example, could reduce the extent to which snap-off occurs, possibly enhancing recoverability. Additionally, a two-component two-phase model was used for simulations. This limits the options for cushion gas to hydrogen. Extending the model to include a third component would enable other gases, such as methane or nitrogen, to serve as cushion gas. Another option for future work is the incorporation of electricity supply profiles. Ultimately, these then determine the rates and durations of injection and production cycles.

This work has demonstrated that hydrogen is recoverable from field-scale reservoirs. For a more comprehensive assessment of the feasibility of subsurface hydrogen storage, future work should incorporate hydrogen supply chains and techno-economic considerations. In this way, the technique can be qualitatively compared to other forms of large-scale energy storage.

References

[1] Abou-Kassem, J. H. et al. *Petroleum reservoir simulation: the engineering approach*. Elsevier, 2020.

[2] Alva, G. et al. "An overview of thermal energy storage systems". In: *Energy* 144 (2018), pp. 341–378. ISSN: 0360-5442. DOI: https://doi.org/10.1016/j.energy.2017.12.037.

[3] Aziz, K. and Settari, A. *Petroleum Reservoir Simulation*. Society of Petroleum Engineers, 1979. ISBN: 978-1-61399-964-6. DOI: https://doi.org/10.2118/9781613999646.

[4] Barelli, L. et al. "Hydrogen production through sorption-enhanced steam methane reforming and membrane technology: A review". In: *Energy* 33.4 (2008), pp. 554–570. ISSN: 0360-5442. DOI: https://doi.org/10.1016/j.energy.2007.10.018.

[5] Bear, J. *Dynamics of fluids in porous media*. Courier Corporation, 1972.

[6] *BGS Lexicon of Named Rock Units: Ness Formation*. https://webapps.bgs.ac.uk/lexicon/lexicon.cfm?pub=NESS.

[7] *BGS Lexicon of Named Rock Units: Tarbert Formation*. https://webapps.bgs.ac.uk/lexicon/lexicon.cfm?pub=TARB.

[8] Blair, P. and Weinaug, C. "Solution of Two-Phase Flow Problems Using Implicit Difference Equations". In: *Society of Petroleum Engineers Journal* 9.04 (Dec. 1969), pp. 417–424. ISSN: 0197-7520. DOI: https://doi.org/10.2118/2185-PA.

[9] Bosma, S. et al. "Multiscale finite volume method for discrete fracture modeling on unstructured grids (MS-DFM)". In: *Journal of Computational Physics* 351 (2017), pp. 145–164. ISSN: 0021-9991. DOI: https://doi.org/10.1016/j.jcp.2017.09.032.

[10] Brauns, J. and Turek, T. "Alkaline Water Electrolysis Powered by Renewable Energy: A Review". In: *Processes* 8.2 (2020). ISSN: 2227-9717. DOI: https://doi.org/10.3390/pr8020248.

[11] Brooks, R. H. *Hydraulic properties of porous media*. Colorado State University, 1965.

[12] Caglayan, D. G. et al. "Technical potential of salt caverns for hydrogen storage in Europe". In: *International Journal of Hydrogen Energy* 45.11 (2020), pp. 6793–6805. ISSN: 0360-3199. DOI: https://doi.org/10.1016/j.ijhydene.2019.12.161.

[13] *Simulation of Relative Permeability Hysteresis to the Nonwetting Phase*. Vol. SPE Annual Technical Conference and Exhibition. SPE Annual Technical Conference and Exhibition. Oct. 1981, SPE-10157–MS. DOI: https://doi.org/10.2118/10157-MS.

[14] Chamock, M. et al. "Sequence Stratigraphy of the Lower Jurassic Dunlin Group, Northern North Sea". In: *Sedimentary Environments Offshore Norway Palaeozoic to Recent*. Ed. by Martinsen, O. J. and Dreyer, T. Vol. 10. Norwegian Petroleum Society Special Publications. Elsevier, 2001, pp. 145–174. DOI: https://doi.org/10.1016/S0928-8937(01)80012-6.

[15] Chen, H. et al. "Progress in electrical energy storage system: A critical review". In: *Progress in Natural Science* 19.3 (2009), pp. 291–312. ISSN: 1002-0071. DOI: https://doi.org/10.1016/j.pnsc.2008.07.014.

[16] Corey, A. T. “The interrelation between gas and oil relative permeabilities”. In: *Producers monthly* (1954), pp. 38–41.

[17] Darcy, H. *Les fontaines publiques de la ville de Dijon: Exposition et application des principes à suivre et des formules à employer dans les questions de distribution d'eau*. Vol. 2. Victor Dalmont, éditeur, 1856.

[18] Darling, R. M. “Techno-economic analyses of several redox flow batteries using levelized cost of energy storage”. In: *Current Opinion in Chemical Engineering* 37 (2022), p. 100855. ISSN: 2211-3398. DOI: https://doi.org/10.1016/j.coche.2022.100855.

[19] Delft High Performance Computing Centre (DHPC). DelftBlue Supercomputer (Phase 2). 2024. URL: https://www.tudelft.nl/dhpc/ark:/44463/DelftBluePhase2.

[20] Di Carlo, A. et al. “Photovoltaics”. In: *EPJ Web Conf.* 246 (2020), p. 00005. DOI: https://doi.org/10.1051/epjconf/202024600005.

[21] Eigestad, G. T. et al. “Geological modeling and simulation of CO2 injection in the Johansen formation”. In: *Computational Geosciences* 13.4 (2009), pp. 435–450. DOI: https://doi.org/10.1007/s10596-009-9153-y.

[22] Engquist, B. *Encyclopedia of applied and computational mathematics*. Springer Berlin, 2015.

[23] Foh, S. et al. *Underground hydrogen storage. Final report. [Salt caverns, excavated caverns, aquifers and depleted fields]*. Tech. rep. Brookhaven National Lab., Upton, NY (USA), Nov. 1979. DOI: https://doi.org/10.2172/6536941.

[24] Garrett, S. *Introduction to actuarial and financial mathematical methods*. Academic Press, 2015.

[25] Gassnova. *CLIMIT Programme*. https://gassnova.no/en/climit-programme. 2025.

[26] Grigoriev, S. et al. “Current status, research trends, and challenges in water electrolysis science and technology”. In: *International Journal of Hydrogen Energy* 45.49 (2020). Progress in Hydrogen Production and Utilization, pp. 26036–26058. ISSN: 0360-3199. DOI: https://doi.org/10.1016/j.ijhydene.2020.03.109.

[27] Hauch, A. et al. “Recent advances in solid oxide cell technology for electrolysis”. In: *Science* 370.6513 (2020), eaba6118. DOI: https://doi.org/10.1126/science.aba6118.

[28] Hopkinson, J. et al. “Effects of Reservoir Heterogeneity on Performance”. In: vol. Fall Meeting of the Society of Petroleum Engineers of AIME. SPE Annual Technical Conference and Exhibition. Oct. 1960, SPE-1581–G. DOI: https://doi.org/10.2118/1581-G.

[29] HosseiniMehr, M. et al. “Projection-based embedded discrete fracture model (pEDFM) on corner-point grid geometry for subsurface flow and geothermal modeling”. In: *ECMOR XVII*. Vol. 2020. 1. European Association of Geoscientists & Engineers. 2020, pp. 1–16. DOI: https://doi.org/10.3997/2214-4609.202035245.

[30] International Energy Agency (IEA). *Renewables 2024: Analysis and Forecast to 2028*. 2024. URL: https://iea.blob.core.windows.net/assets/17033b62-07a5-4144-8dd0-651cdb6caa24/Renewables2024.pdf.

[31] International Energy Agency (IEA). *Hydrogen*. IEA Energy System Low-Emission Fuels. 2025. URL: https://www.iea.org/energy-system/low-emission-fuels/hydrogen.

[32] International Renewable Energy Agency (IRENA). *Electricity Storage and Renewables: Costs and Markets to 2030*. 2017. URL: https://www.irena.org/-/media/Files/IRENA/Agency/Publication/2017/Oct/IRENA_Electricity_Storage_Costs_2017_Summary.pdf.

[33] Jafari Raad, S. M. et al. “Hydrogen storage in saline aquifers: Opportunities and challenges”. In: *Renewable and Sustainable Energy Reviews* 168 (2022), p. 112846. ISSN: 1364-0321. DOI: https://doi.org/10.1016/j.rser.2022.112846.

[34] Jansen, J. D. *A systems description of flow through porous media*. Vol. 570. Springer, 2013.

[35] Jenny, P. et al. “Adaptive fully implicit multi-scale finite-volume method for multi-phase flow and transport in heterogeneous porous media”. In: *Journal of Computational Physics* 217.2 (2006), pp. 627–641. ISSN: 0021-9991. DOI: https://doi.org/10.1016/j.jcp.2006.01.028.

[36] Junginger, M. et al. “Chapter 6 - Onshore wind energy”. In: *Technological Learning in the Transition to a Low-Carbon Energy System*. Ed. by Junginger, M. and Louwen, A. Academic Press, 2020, pp. 87–102. ISBN: 978-0-12-818762-3. DOI: https://doi.org/10.1016/B978-0-12-818762-3.00006-6.

[37] Kanaani, M. et al. “Role of Cushion Gas on Underground Hydrogen Storage in Depleted Oil Reservoirs”. In: *Journal of Energy Storage* 45 (2022), p. 103783. ISSN: 2352-152X. DOI: https://doi.org/10.1016/j.est.2021.103783.

[38] Kebede, A. A. et al. “A comprehensive review of stationary energy storage devices for large scale renewable energy sources grid integration”. In: *Renewable and Sustainable Energy Reviews* 159 (2022), p. 112213. ISSN: 1364-0321. DOI: https://doi.org/10.1016/j.rser.2022.112213.

[39] Khodadoost Arani, A. et al. “Review of Flywheel Energy Storage Systems structures and applications in power systems and microgrids”. In: *Renewable and Sustainable Energy Reviews* 69 (2017), pp. 9–18. ISSN: 1364-0321. DOI: https://doi.org/10.1016/j.rser.2016.11.166.

[40] Killough, J. “Reservoir Simulation With History-Dependent Saturation Functions”. In: *Society of Petroleum Engineers Journal* 16.01 (Feb. 1976), pp. 37–48. ISSN: 0197-7520. DOI: https://doi.org/10.2118/5106-PA.

[41] Li, G. and Yao, J. “Snap-Off during Imbibition in Porous Media: Mechanisms, Influencing Factors, and Impacts”. In: *Eng* 4.4 (2023), pp. 2896–2925. ISSN: 2673-4117. URL: https://www.mdpi.com/2673-4117/4/4/163.

[42] Lie, K. A. *An introduction to reservoir simulation using MATLAB: user guide for the Matlab Reservoir Simulation Toolbox (MRST)*. Vol. 118. Departement of Applied Mathematics Oslo, Norway, 2016.

[43] Lomeland, F. et al. “A New Versatile Relative Permeability Correlation”. In: Aug. 2005.

[44] Lord, A. S. et al. “Geologic storage of hydrogen: Scaling up to meet city transportation demands”. In: *International Journal of Hydrogen Energy* 39.28 (2014), pp. 15570–15582. ISSN: 0360-3199. DOI: https://doi.org/10.1016/j.ijhydene.2014.07.121.

[45] Ly, S. et al. “Newton-Raphson Method: Overview and Applications”. In: *Advances in Decision Sciences* 28.3 (Sept. 2024), pp. 1–26. URL: https://www.proquest.com/scholarly-journals/newton-raphson-method-overview-applications/docview/3201851015/se-2.

[46] Lysyy, M. et al. “Hydrogen Relative Permeability Hysteresis in Underground Storage”. In: *Geophysical Research Letters* 49.17 (2022), e2022GL100364. DOI: https://doi.org/10.1029/2022GL100364.

[47] McCarty, R. D. *Selected properties of hydrogen (engineering design data)*. Vol. 168. US Department of Commerce, National Bureau of Standards, 1981.

[48] Meenal, R. et al. “Weather Forecasting for Renewable Energy System: A Review”. In: *Archives of Computational Methods in Engineering* 29.5 (2022), pp. 2875–2891. DOI: 10.1007/s11831-021-09695-3.

[49] Miocic, J. et al. “Underground hydrogen storage: a review”. In: *Geological Society, London, Special Publications* 528.1 (2023), pp. 73–86. DOI: https://doi.org/10.1144/SP528-2022-88.

[50] Molburg, J. C. and Doctor, R. D. “Hydrogen from steam-methane reforming with CO2 capture”. In: *20th annual international Pittsburgh coal conference*. Vol. 20. 2003, pp. 1–20.

[51] Moukalled, F. et al. *The Finite Volume Method in Computational Fluid Dynamics*. Springer, 2016.

[52] Muhammed, N. S. et al. “Hydrogen storage in depleted gas reservoirs: A comprehensive review”. In: *Fuel* 337 (2023), p. 127032. ISSN: 0016-2361. DOI: https://doi.org/10.1016/j.fuel.2022.127032.

[53] Musial, W. et al. “Energy From Offshore Wind”. In: vol. Offshore Technology Conference. OTC Offshore Technology Conference. May 2006, OTC-18355–MS. DOI: https://doi.org/10.4043/18355-MS.

[54] *National Institute of Standards and Technology — nist.gov*. https://www.nist.gov/.

[55] Oldenburg, C. M. et al. “Water Upconing in Underground Hydrogen Storage: Sensitivity Analysis to Inform Design of Withdrawal”. In: *Transport in Porous Media* 151.1 (Jan. 2024), pp. 55–84. ISSN: 1573-1634. DOI: https://doi.org/10.1007/s11242-023-02033-0.

[56] *OpenGoSim Documentation: GRDECL Grid Format*. https://docs.opengosim.com/manual/input_deck/grid/grdecl/. 2025.

[57] Pilali, E. et al. “SWOT analysis on the transition from Lithium-Ion batteries to Sodium-Ion batteries”. In: *Sustainable Energy Technologies and Assessments* 80 (2025), p. 104371. ISSN: 2213-1388. DOI: https://doi.org/10.1016/j.seta.2025.104371.

[58] Plohr, B. et al. “Modeling hysteresis in porous media flow via relaxation”. In: *Computational Geosciences* 5.3 (2001), pp. 225–256. DOI: https://doi.org/10.1023/A:1013759420009.

[59] Ponting, D. K. “Corner point geometry in reservoir simulation”. In: *ECMOR I-1st European conference on the mathematics of oil recovery*. European Association of Geoscientists & Engineers. 1989, cp–234. DOI: https://doi.org/10.3997/2214-4609.201411305.

[60] Rahman, M. J. et al. “Lateral distribution of the upper Amundsen shale in potential CO2 storage site Aurora, northern North Sea”. In: *Proceedings of the 16th Greenhouse Gas Control Technologies Conference (GHGT-16)*. 2022, pp. 23–24. DOI: http://dx.doi.org/10.2139/ssrn.4284857.

[61] Rao, P. C. and Yoon, M. “Potential Liquid-Organic Hydrogen Carrier (LOHC) Systems: A Review on Recent Progress”. In: *Energies* 13.22 (2020). ISSN: 1996-1073. DOI: https://doi.org/10.3390/en13226040.

[62] Revankar, S. T. “Chapter Six - Chemical Energy Storage”. In: *Storage and Hybridization of Nuclear Energy*. Ed. by Bindra, H. and Revankar, S. Academic Press, 2019, pp. 177–227. ISBN: 978-0-12-813975-2. DOI: https://doi.org/10.1016/B978-0-12-813975-2.00006-5.

[63] Rochelle, G. T. “Amine Scrubbing for CO_2 Capture”. In: *Science* 325.5948 (2009), pp. 1652–1654. DOI: https://doi.org/10.1126/science.1176731.

[64] van Rooijen, W. A. and Hajibeygi, H. “Site Selection for Underground Hydrogen Storage in Porous Media: Critical Review and Outlook”. In: *Energy & Fuels* (Sept. 2025). ISSN: 0887-0624. DOI: https://doi.org/10.1021/acs.energyfuels.5c03665.

[65] Rusman, N. and Dahari, M. “A review on the current progress of metal hydrides material for solid-state hydrogen storage applications”. In: *International Journal of Hydrogen Energy* 41.28 (2016), pp. 12108–12126. ISSN: 0360-3199. DOI: https://doi.org/10.1016/j.ijhydene.2016.05.244.

[66] Sezer, N. et al. “A comprehensive review of the state-of-the-art of proton exchange membrane water electrolysis”. In: *Materials Science for Energy Technologies* 8 (2025), pp. 44–65. ISSN: 2589-2991. DOI: https://doi.org/10.1016/j.mset.2024.07.006.

[67] SINTEF. *MatMoRA: Material Risk Assessment of CO_2 Storage (2007–2011)*. https://www.sintef.no/projectweb/matmora/matmora-2007-2011/. 2011.

[68] Sircar, S. "Pressure Swing Adsorption". In: *Industrial & Engineering Chemistry Research* 41.6 (2002), pp. 1389–1392. ISSN: 0888-5885. DOI: https://doi.org/10.1021/ie0109758.

[69] *SPE Comparative Solution Project: Problem Set 2*. https://www.spe.org/web/csp/datasets/set02.htm. Society of Petroleum Engineers. 2001.

[70] Statistics Netherlands (CBS). *Over Half of Electricity Production Now Comes from Renewable Sources*. 2024. URL: https://www.cbs.nl/en-gb/news/2024/39/over-half-of-electricity-production-now-comes-from-renewable-sources.

[71] Steffy, D. A. et al. "Influence of antecedent moisture content on residual LNAPL Saturation". In: *Journal of Soil Contamination* 6.2 (1997), pp. 113–147. DOI: https://doi.org/10.1080/15320389709383552.

[72] Stone, H. B. J. et al. "Underground hydrogen storage in the UK". In: *Underground Gas Storage: Worldwide Experiences and Future Development in the UK and Europe*. Geological Society of London, Jan. 2009. ISBN: 9781862392724. DOI: https://doi.org/10.1144/SP313.13.

[73] Sundal, A. et al. "The Lower Jurassic Johansen Formation, northern North Sea Depositional model and reservoir characterization for CO2 storage". In: *Marine and Petroleum Geology* 77 (2016), pp. 1376–1401. ISSN: 0264-8172. DOI: https://doi.org/10.1016/j.marpetgeo.2016.01.021.

[74] Sweeney, C. et al. "The future of forecasting for renewable energy". In: *WIREs Energy and Environment* 9.2 (2020), e365. DOI: https://doi.org/10.1002/wene.365.

[75] TNO. *B10011 Report*. 2024. URL: https://publications.tno.nl/publication/34627904/P1i42V/b10011.pdf.

[76] Töpler, J. and Lehmann, J. "Hydrogen and fuel cell". In: *Technologies and Market Perspectives. Springer, Berlin* (2016).

[77] U.S. Department of Energy, Hydrogen and Fuel Cell Technologies Office. *Hydrogen Storage*. U.S. Department of Energy. URL: https://www.energy.gov/eere/fuelcells/hydrogen-storage.

[78] Valenti, G. "2 - Hydrogen liquefaction and liquid hydrogen storage". In: *Compendium of Hydrogen Energy*. Ed. by Gupta, R. B. et al. Woodhead Publishing Series in Energy. Woodhead Publishing, 2016, pp. 27–51. ISBN: 978-1-78242-362-1. DOI: https://doi.org/10.1016/B978-1-78242-362-1.00002-X.

[79] Wang, Y. et al. "Analysis of hydrodynamic trapping interactions during full-cycle injection and migration of CO2 in deep saline aquifers". In: *Advances in Water Resources* 159 (2022), p. 104073. ISSN: 0309-1708. DOI: https://doi.org/10.1016/j.advwatres.2021.104073.

[80] Whitaker, S. "Flow in porous media I: A theoretical derivation of Darcy's law". In: *Transport in porous media* 1.1 (1986), pp. 3–25. DOI: https://doi.org/10.1007/BF01036523.

8

DARSim on DelftBlue

In case one wants to run multiple reservoir simulations in DARSim at once without rendering their laptop unusable, or requires more computing power for their job, DARSim can be run on DelftBlue [19]. It is easy to use, and can be operated in various ways. Here, operation through MobaXterm will be described.

8.1. MobaXterm

MobaXterm is an all-in-one application for remote computing. It can be downloaded through: `https://mobaxterm.mobatek.net/download.html` First, students need to apply for access to DelftBlue through TopDesk. Upon loading MobaXterm, the home screen will show, see Fig. 8.1.

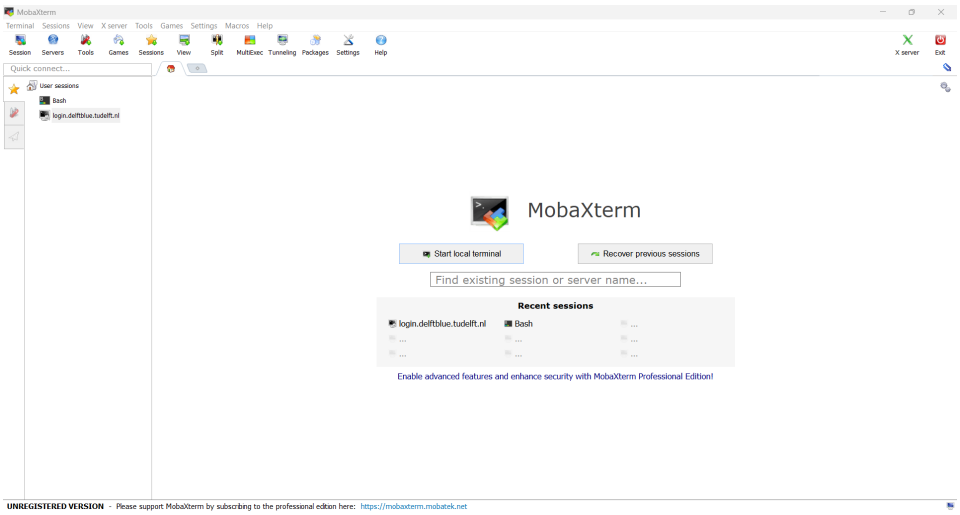

Figure 8.1: MobaXterm home screen.

In the bar that says: 'Find existing session or server name', type: `login.delftblue.tudelft.nl`. Then, log in using your netID and associated password. Now, the DelftBlue welcome screen will show, see Fig. 8.2.

On this screen, there is some information about limitations to disk storage. There are two disks you can use. First there is the `home` disk, which has a limit of 30 GB of storage. This disk is backed up. The other disk is the `scratch` disk, with a storage limit of 5 TB. However, files that have not been modified for over 6 months are automatically removed. Therefore, it is wise to regularly transfer files and folder to your computer. Within the terminal, use command `cd` to change directories.

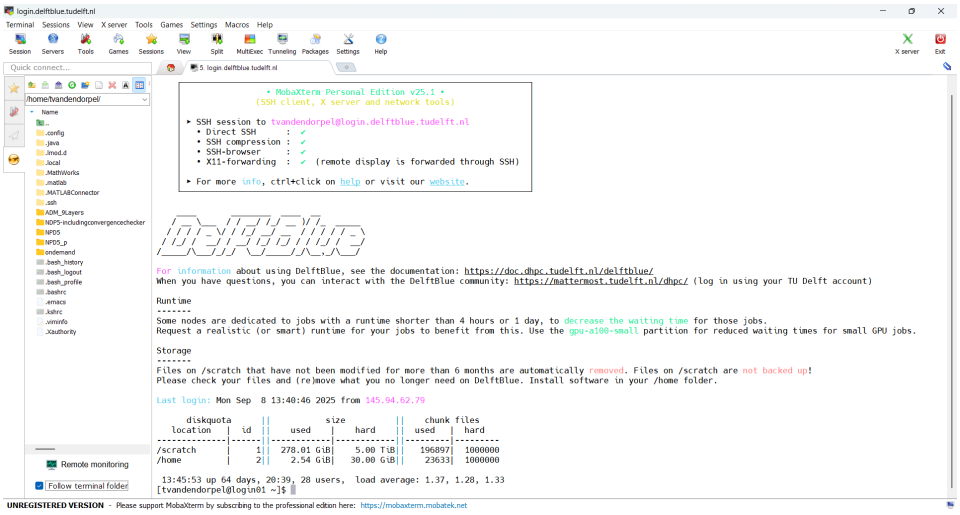

Figure 8.2: DelftBlue welcome screen.

8.1.1. Shell script

On the left in MobaXterm, the path and folders in it are shown. In order to run DARSim now, two extra files need to be added in the `darsim/src/` folder you want to run your simulation from. The first file is a shell script, which contains the information for Slurm to run the job. Slurm is the workload manager that manages jobs in DelftBlue. An example of a shell script is given in Fig. 8.3.

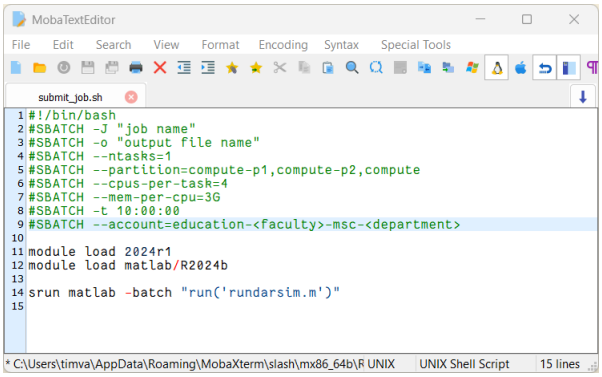

Figure 8.3: Typical structure of a shell script.

Each line will be given a short description now. The first line, `#!/bin/bash`, tells the system which interpreter to use to run the shell script. In this case, the `bash` shell is used, located within `bin`. The second line gives the job a name. This name will show up when running jobs are viewed with the `squeue` or `sacct` commands. The next line specifies the name of the corresponding output file. In the case of DARSim, this output file contains the outputs that are already saved in `RunDiary.txt`. Next, the number of tasks is specified with `ntasks`. The next line specifies which partition should be used. For phase 1 compute nodes, `compute` and `compute-p1` are used. For compute nodes of phase 2, use `compute-p2`. The next two lines set the number of CPUs that are used per task, and the memory each CPU can use. Choosing an appropiate number of CPUs and memory per CPU is beneficial for shorter queueing times. Next, the maximum running time for the job is set. Finally, the account has to be specified. In the email confirming your DelftBlue account from TopDesk, this account will be provided.

Now, a pair of modules has to be loaded. The first line loads the module `2024r1`, which is the default Delft-

Blue software stack. Now, MATLAB can be loaded with `module load matlab/R2024b`. Use the command `module avail` in the terminal to check for the latest version of these modules.
Finally, it can be specified what the job needs to execute. For running a simulation on DARSim, this is specified by:

```
srun matlab -batch "run('rundarsim.m')"
```

First of all, `srun` enables the user to run a job in parallel. Then, `matlab` calls the MATLAB executable. Now the `-batch` flag runs MATLAB and automatically exits after the script has been executed. In this case, the commands it executes is `"run('rundarsim.m')"`.

8.1.2. Executable script

Since the Command Window in MATLAB cannot be used in DelftBlue, another script has to be created within the `darsim/src/` folder. In this script, the command with which DARSim is run on a regular computer is written. The file is structured as follows:

```
DARSim('../../', '<YourCompositionFile>.txt', n)
```

with `n` being the number of nodes used for parallelization of the simulation. Note that this number needs to match the number of assigned CPUs in the shell script.

8.1.3. Running a job

With both files now ready, the job is ready to be run. To do so, move to the `darsim/src/` folder, and run the following command in the terminal: `sbatch <YourShellScript>.sh`. Using the commands `squeue`, active jobs can be monitored. With `sacct`, the status of running and finished jobs can be tracked.

8.2. File transfer

Now that the job is running, the output files will be stored in a separate 'Output' folder within the working directory. To visualize and process these files, they have to be transferred to your device. In MobaXterm, this can be done by dragging and dropping the folders, or by using the 'Download selected files' button above the current path. However, it is faster to use Windows Command Prompt or PowerShell for this, especially when the folders are large in size. Files can be transfered from DelftBlue to your device by the use of the `scp` command. It is used as follows:

```
scp -pr <netID>@login.delftblue.tudelft.nl:/Path/To/FileOrFolder/On/DelftBlue
                                                Path\To\Destination\Folder\On\Device
```

Similarly, files and folders can be transfered from your device to DelftBlue with the following syntax:

```
scp -pr \Path\To\Local\FileOrFolder
        <netID>@login.delftblue.tudelft.nl:/Path/To/Destination/Folder/On/DelftBlue
```